



Insights on fault reactivation during the 2019 November 11, Mw 4.9 Le Teil earthquake in southeastern France, from a joint 3-D geological model and InSAR time-series analysis

Léo Marconato, P H Leloup, C Lasserre, R Jolivet, Séverine Caritg, R Grandin, M Métois, O Cavalié, L Audin

► To cite this version:

Léo Marconato, P H Leloup, C Lasserre, R Jolivet, Séverine Caritg, et al.. Insights on fault reactivation during the 2019 November 11, Mw 4.9 Le Teil earthquake in southeastern France, from a joint 3-D geological model and InSAR time-series analysis. *Geophysical Journal International*, 2021, 229 (2), pp.758 - 775. 10.1093/gji/ggab498 . hal-03573241

HAL Id: hal-03573241

<https://univ-lyon1.hal.science/hal-03573241>

Submitted on 14 Feb 2022

HAL is a multi-disciplinary open access archive for the deposit and dissemination of scientific research documents, whether they are published or not. The documents may come from teaching and research institutions in France or abroad, or from public or private research centers.

L'archive ouverte pluridisciplinaire **HAL**, est destinée au dépôt et à la diffusion de documents scientifiques de niveau recherche, publiés ou non, émanant des établissements d'enseignement et de recherche français ou étrangers, des laboratoires publics ou privés.

**Insights on fault reactivation during the November 11, 2019, M_w4.9 Le Teil
earthquake in south-eastern France, from a joint 3D geological model and
InSAR time series analysis**

L. Marconato ¹, P. H. Leloup ¹, C. Lasserre ¹, R. Jolivet ^{2,3}, S. Caritg ⁴, R. Grandin ⁵,
M. Métois ¹, O. Cavalié ^{1,6}, L. Audin ⁷

¹ Univ Lyon, Univ Lyon 1, ENSL, CNRS, LGL-TPE, F-69622, Villeurbanne, France

² Laboratoire de Géologie, Département de Géosciences, École Normale Supérieure, PSL Université, CNRS UMR 8538, Paris, France

³ Institut Universitaire de France, 1 rue Descartes, 75006 Paris, France

⁴ Bureau de Recherches Géologiques et Minières (BRGM), France

⁵ Université de Paris, Institut de physique du globe de Paris, CNRS, F-75005 Paris, France

⁶ Université Côte d'Azur, IRD, CNRS, Observatoire de la Côte d'Azur, Géoazur, France

⁷ ISTerre, Univ. Grenoble Alpes, CNRS, IRD, Grenoble, France

Manuscript accepted for publication by GJI: <https://doi.org/10.1093/gji/ggab498>

Abbreviated title: 3D geology and InSAR study of the 2019 Le Teil earthquake

Corresponding author: Léo Marconato, leo.marconato@ens-lyon.fr

28 **Summary**

29 The 2019, Mw4.9 Le Teil earthquake occurred in south-eastern France, causing substantial damage in this
30 slow deforming region. Field observations, remote sensing and seismological studies following the event
31 revealed that coseismic slip concentrates at shallow depth along a ~5 km long rupture associated with surface
32 breaks and a thrusting mechanism. We further investigate this earthquake by combining geological field
33 mapping, 3D geology, InSAR time series analysis and a coseismic slip inversion. From structural, stratigraphic
34 and geological data collected around the epicenter, we first produce a 3D geological model of the region
35 surrounding the rupture using the GeoModellerTM software. Our model includes the geometry of the geological
36 layers and of the main faults, including the La Rouvière Fault, the Oligocene normal fault that ruptured during
37 the earthquake. We generate a time series of surface displacement from Sentinel-1 SAR data ranging from
38 early January 2019 to late January 2020 using the NSBAS processing chain. The spatio-temporal patterns of
39 surface displacement for this time span show neither a clear pre-seismic signal nor significant post-seismic
40 transient deformation. We extract the coseismic displacement pattern from the InSAR time series, highlighting
41 along-strike variations of coseismic surface slip. The maximum relative displacement along the Line-Of-Sight
42 is up to ~16 cm and is located in the southwestern part of the rupture. We invert for the slip distribution on the
43 fault from the InSAR coseismic surface displacement field. Constraining our fault geometry from the
44 geological model, acceptable fault dip ranges between 55° and 60°. Our model confirms the reactivation of La
45 Rouvière fault, with reverse slip at very shallow depth and two main slip patches reaching respectively 30 cm
46 and 24 cm of slip, both around 500 m depth. We finally discuss how the 3D fault geometry and geological
47 structure may have impacted the slip distribution and propagation during the earthquake. This study is a step
48 to reassess the seismic hazard of the many faults similar to the La Rouvière one along the Cévennes fault
49 system, in a densely populated area hosting several sensitive nuclear sites.

50
51
52
53
54

Key words: Continental neotectonics; Seismic cycle; Radar interferometry; Time-series analysis; Earthquake
source observations; Inverse theory

55 1 Introduction

56 On the 11th of November 2019, the Mw4.9 Le Teil earthquake struck the region of Montélimar, in the
57 western Rhône valley in South-East France (**Fig. 1a**). The towns of Le Teil, Saint-Thomé, and Viviers, all
58 located in the epicentral area, suffered important economic damages (~50M€). Thankfully, only a small
59 number of injured people were reported. Partial building collapse happened in a radius of about 10 km
60 corresponding to macroseismic intensities of VII to VIII (EMS98; Cornou et al., 2020). The earthquake caused
61 the temporary shutdown of a nuclear power plant located 15 km to the north of the epicenter for security check.

62 The first epicentral localizations obtained by seismological institutes all being inaccurate by several
63 kilometers (**Fig. 1b**), it is the first Sentinel-1 interferograms that allowed a precise localization of the Le Teil
64 earthquake (Cornou et al., 2020). These interferograms show a sharp surface rupture (Ritz et al., 2020)
65 suggesting that the earthquake ruptured the La Rouvière Fault (LRF), a normal fault previously mapped
66 (Kerrien et al. 1989) and considered inactive since the Oligocene. The reverse-faulting and very shallow (< 3
67 km) focal mechanisms estimates matched InSAR imagery, suggesting a reactivation of the shallow part of the
68 LRF in reverse motion, hence with an inversion of its kinematics. In addition, the strong mobilization of the
69 French scientific community (Delouis et al., 2019; Cornou et al., 2020), guided by InSAR imagery, led to the
70 identification of several surface breaks associated with the Le Teil event, matching both the preliminary trace
71 inferred from InSAR data and the previously mapped trace of the LRF (Ritz et al., 2020) (**Fig. 1b**). Up to 13
72 cm of surface displacement was measured on the field, and InSAR suggested up to 15 cm of relative surface
73 motion.

74 The occurrence of such shallow reverse faulting earthquake along a previously thought to be inactive
75 normal fault raises several issues. The reactivation of the LRF must be examined in the light of the geological
76 context and the fault geometry. In addition, the potential triggering of the event by the surface unloading
77 induced by excavation in a cement quarry located in the immediate vicinity of the LRF is still debated
78 (Ampuero et al., 2020; De Novellis, 2020). The hypothesis of excavation induced triggering is favoured by the
79 very shallow depth of the event and the lack of aftershock (Delouis et al., 2019). The reassessment of the
80 seismic hazard zoning must also be considered in the whole Ardèche margin where faults similar to the LRF
81 are collocated with several nuclear facilities and populated areas.

82 From a more fundamental point of view, as fault geometry and geological, lithological and structural
83 inheritance appear to be key factors to understand the extent and the variability of slip during earthquakes (e.g.
84 King & Nabelek, 1985; Wesnousky, 2006; Choi et al., 2018), the Le Teil earthquake represents a rare
85 opportunity to study the interaction between pre-existing geological 3D structures and earthquake deformation
86 in a slow deforming context. The very shallow slip distribution of this rather small event allows to put together
87 different geological and geodetic datasets at a resolution (hundreds of meters) at which larger earthquake
88 ruptures can hardly be studied.

89 We investigate the Le Teil earthquake combining field mapping, 3D structural and geological
90 modeling, InSAR time series analysis and inversion for coseismic slip distribution. First, from field mapping,
91 we constrain the geological formations and faults around the epicentral area and produce a 3D numerical model
92 of the geological layers and faults, including the LRF. Then, we compute a one-year InSAR Sentinel-1 time
93 series, covering ten months prior and three months after the earthquake, in order to both refine the spatial
94 coverage of the coseismic displacement map in the near field and investigate whether pre-seismic deformation
95 or afterslip may have occurred or not. We model the slip distribution using the surface deformation field of the
96 Le Teil earthquake. We compare our slip distribution with the geological and morphological features of the
97 area. This multi-disciplinary approach provides constraints about the geometry of the LRF, opening the
98 discussion on the potential factors that controlled the reactivation of the fault and on the need to reassess
99 seismic hazard in this region.

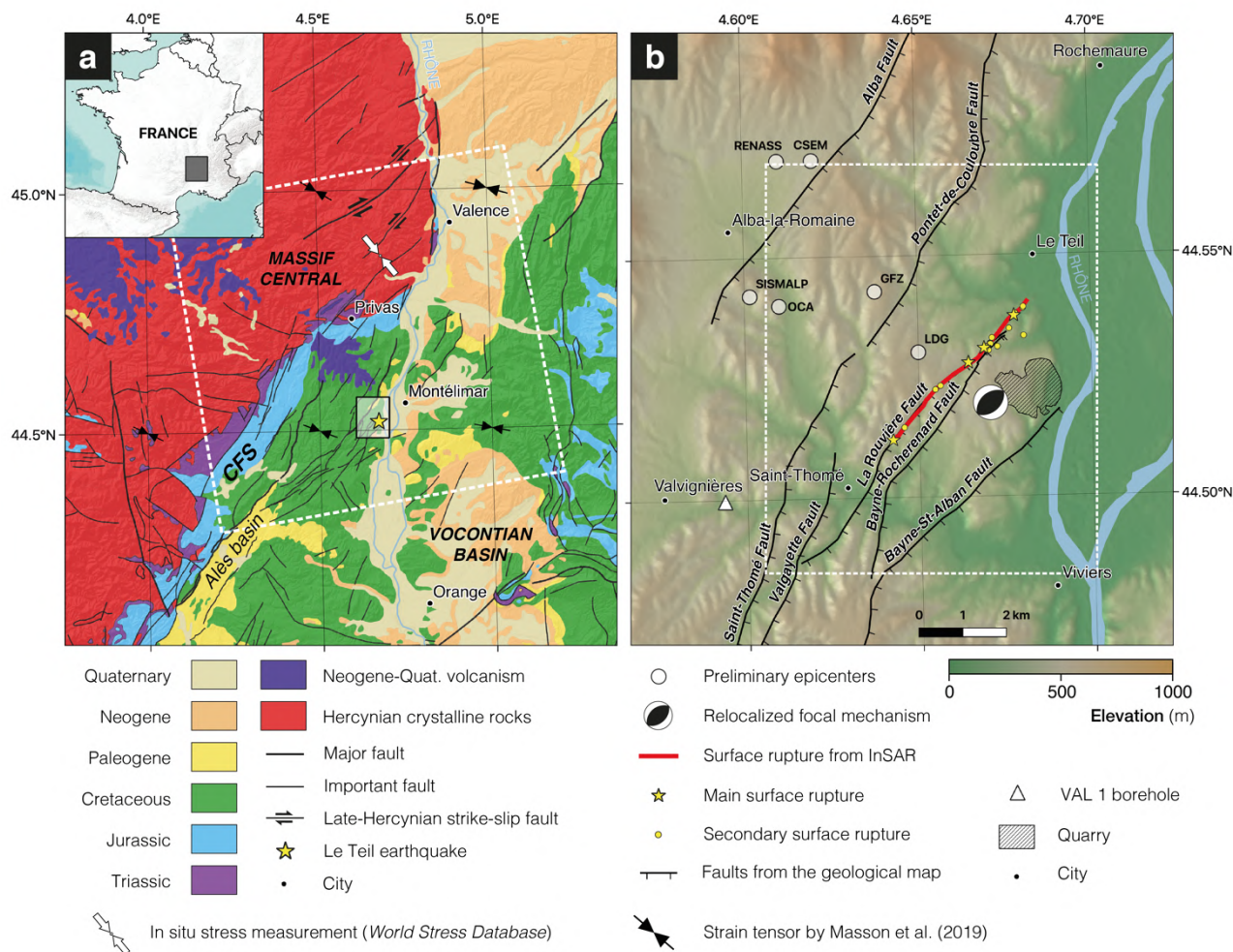


Figure 1. Geological and seismotectonic setting of the Le Teil earthquake. (a) Regional geological and structural map (Chantraine et al., 1996). Black arrows show the principal horizontal compressive directions of the strain tensor (Masson et al., 2019). White dashed outline shows coverage of reprocessed InSAR data. Black rectangle shows the extent of b. (b) Surface rupture trace is in red. Yellow dots indicating location of field observations of coseismic displacement from Ritz et al (2020). Faults in black are from Saint Martin (2009). Rectangle in dotted white in panel b show coverage of the 3D geological model in Fig. 2. Revised location of epicenter (yellow star in a) and focal mechanism are from Delouis et al. (2021).

110 2 Geological and structural history of Le Teil area

111 The Le Teil earthquake occurred in the so-called Vivaro-Cévenole margin in between the Hercynian
112 crystalline basement of the Massif Central to the NW, and the Vocontian Mesozoic basin to the SE (**Fig. 1a**).
113 The margin between these two domains corresponds to a ~900 m topographic change and a network of NE-
114 SW faults that runs for more than 150 km from the Bas Dauphiné to the Languedoc. This fault network, called
115 the Cévennes fault system (CFS), shows evidence for a long and polyphased structural history with
116 compression, strike-slip and extension phases during the Paleozoic, extension phases during the Mesozoic and
117 extension and compression phases during the Cenozoic.

118 NW-SE faults with apparent dextral offset affect the basement but not the Mesozoic cover (**Fig. 1a**)
119 (e.g., Chantraine et al., 2006) and are interpreted as Late Hercynian strike-slip faults (Arthaud & Matte, 1975;
120 Chardon et al., 2020) that may have been reactivated during the later deformation phases. The end of the
121 Hercynian orogenic cycle corresponds to a carboniferous phase of detrital sediments and coal deposit as well
122 as several deformation phases. Widespread erosion was then followed by the deposit of Triassic continental
123 sediments. During the Mesozoic more than 10 km of marine sediments accumulated in the Vocontian basin.
124 At that time, the Vivaro-Cévenole margin corresponded to a network of NW-SE synsedimentary normal faults
125 delimiting tilted blocks (Elmi et al, 1983; 1996; Soechting, 1996). The precise mode and direction of extension
126 varied through time with three extension stages: Middle Triassic pre-rift, Early-Middle Jurassic Thethysian
127 rifting, and Late Jurassic-Early Cretaceous thermal subsidence (Elmi et al., 1983; Bonijoly et al., 1996). From
128 the interpretation of three seismic lines, a gravimetry map, and two deep boreholes located ~25 km west of Le
129 Teil (**Fig. 1a**), Bonijoly et al. (1996) propose a WNW-ESE balanced cross-section of the Vivaro-Cévenole
130 margin. That section shows normal faults, mostly dipping to the SE, rooting on a SE dipping decollement
131 within Carboniferous coal levels. Microstructural studies in the same area indicate a Triassic E-W extension
132 (Bergerat & Martin, 1993) and a Lower Jurassic N-S extension, while the main normal faults strike ~N30
133 (Bergerat & Martin, 1994; Martin & Bergerat, 1996). At other locations along the Vivaro-Cévenole margin,
134 the Lower Jurassic extension is considered to trend NW-SE, in better accordance with NE-SW striking normal
135 faults (Bles et al., 1989 and references therein). The Lower Cretaceous corresponds to the widespread
136 sedimentation of the so-called Urgonian carbonate platform in the Vocontian basin, in a N-S extension context

137 (Bles et al., 1989 and references therein). Thermal modeling of Apatite fission track ages of samples from the
138 Cévennes suggest that Mesozoic sedimentation extended further to the West than the present-day cover-
139 basement boundary, but was eroded before the Upper Cretaceous (Barbaran et al., 2001; Gautheron et al.,
140 2009).

141 Starting from the Aptian, sedimentation becomes detrital, probably because of local regression under
142 far-field effects of the so-called Pyrenean N-S compression. At that time, the CFS was a left-lateral ramp
143 bounding to the west the shortened cover with an ~17 km offset of Upper Jurassic recifal facies in the south
144 (Bodeur, 1976). Associated NE-SW to N-S shortening occurred along several thrusts with decollements in the
145 Triassic evaporites and Mesozoic marls (Arthaud & Laurent, 1995; Arthaud & Séguret, 1981).

146 At the end of the Eocene and during the Oligocene, rift basins straddle across western Europe from
147 the North Sea to the Mediterranean Sea, contemporaneously with compression in the Western Alps, opening
148 of the Golfe du Lion, and volcanism in the Massif Central (Illies, 1972; Bergerat, 1987; Serane et al., 1995;
149 Dezes et al., 2004). At this time NW-SE extension prevails along the CFS, and several NE-SW normal faults
150 are activated (Bles et al., 1989; Roure et al., 1992; and references therein). Some of the faults bound narrow
151 rift basins filled with Oligocene deposits, the largest being the Alès basin (**Fig. 1a**) which is bounded by a
152 major SE dipping fault (Arene et al., 1978). At the surface, the Alès fault dips 35° to the ESE but appears along
153 seismic profiles as a ~15° dipping fault at depth (Roure et al., 1992; Sanchis & Séranne, 2000). The latest study
154 considers that this fault has been active during a two stages extension history starting in the Eocene (Ludian)
155 and connects with a decollement level in the Triassic (Sanchis & Séranne, 2000). Further North, the CFS
156 appears to splay out, with the Lagorce-Vallon, La-Fare-Pontet-de-Couloubre and Larnar-Bayne-St-Alban
157 faults (**Fig. 1a, Fig. 2**). Oligocene sediments were found in the hanging-wall (at SE) of some of these faults at
158 Ellieux (Larnas F.), Couijanet (Baynes-St-Alban F.) and Rochemaure (Pontet-de-Couloubre F.) (**Fig. 1a; Fig.**
159 **2**; Kerrien et al., 1989), suggesting that the faults are Oligocene normal faults. From a balanced cross-section
160 across that part of the margin, Roure et al. (1992; 1994) (**Fig. 1a**) interpret the westernmost faults of the margin
161 to be Lower Jurassic normal faults rooted in the Carboniferous, and the easternmost ones as Oligocene faults
162 partly reactivating Lower Jurassic normal faults but rooted in the Triassic. The Bayne-St-Alban fault possibly
163 connects with the Marsanne fault on the other side of the Rhône River that also separates Mesozoic from
164 Oligocene sediments (**Fig. 1a**). The Pontet de Couloubre fault continues further NE and possibly connects with

165 the Valence fault that bounds a thick Eocene-Oligocene half graben buried below Plio-quaternary and Miocene
166 sediments (Deville et al., 1994; Kalifi, 2021). The Le Teil area is thus located in a relay zone between the N5
167 trending Valence and the N40 trending Alès Oligocene normal faults (**Fig. 1a**).

168 During the Miocene, continental and marine sedimentation takes place in the Rhodano-provençal
169 flexural basin coevally with intense folding and thrusting at the front of the western Alps (**Fig. 1a**) (Ford &
170 Lickorish, 2004). In the Le Teil area, the Oligocene sediments are affected, together with the underlying
171 Mesozoic sediments, by NNE-SSW folds: the Rochemaure and Bayne synclines (**Fig. 2**), and the Serre des
172 Parts and Vivier anticlines (Elmi et al., 1996). As this compression appears to be mostly visible in the eastern
173 part of the zone, it was termed “Rhodanian” and attributed to a Miocene compression (Elmi et al., 1996). Open
174 folds and brittle faults affecting the Miocene molasse of Bas-Dauphiné also implies WNW-ESE to E-W
175 compression (Blès & Gros, 1991). Such mild Late Miocene compression, also affecting most of the Massif
176 Central, would be a far-field effect of the Alpine collision (Blès et al., 1989; Blès & Gros, 1991; and references
177 therein). At the end of the Miocene, between 7.7 and 6.4 Ma effusive basaltic volcanism produced lava flows
178 that reached Rochemaure less than 10 km north of Le Teil (Feraud, 1979; Bandet et al., 1974) (**Fig. 1a**).
179 Contemporaneous dykes are mostly vertical and strike between N110 and N150 with a maximum between
180 N135 and N150° and are compatible with a compression of that direction (Feraud & Campredon, 1983).

181 Post-Pliocene normal faults imply an E-W to NE-SW extension in Bas-Dauphiné that would result
182 from a transcurrent state of stress with sigma 1 trending N-S to NW-SE and sigma 3 trending E-W to NE-SW
183 (Blès & Gros, 1991). Because the southern part of the CFS has a clear geomorphic trace and offsets left-
184 laterally valleys and Quaternary terraces, it has been interpreted to be active with an average slip rate of 0.1-2
185 mm/yr (Lacassin et al., 1998a). Such conclusion is controversial and has stirred up intense scientific discussion
186 (Ambert et al., 1998; Mattauer, 1998; Sébrier et al., 1998; Lacassin et al., 1998b). The Nîmes fault, located
187 ~40 km to the SE, shares nearly the same trend and is considered as active (Grelet et al., 1993; Sébrier, 1997).
188 While the paleo-seismic record is very sparse in France, a paleoearthquake was identified on the Nîmes fault
189 in Courthézon, 50 km south of Le Teil, associated with reverse offsets on a ~N50 oriented fault (Carbon et al.,
190 1993). The most recent synthesis of active faults in France considers the Nîmes fault as a Quaternary fault and
191 the Alès basin border fault, as well as segments of the Pontet-de-Couloubre and Marsanne faults, as potentially
192 active (**Fig. 1**; Jomard et al., 2017).

193 The SISFRANCE database on historical seismicity (sisfrance.net) reveals several earthquake swarms
194 in 1773, 1873 and 1933-36, with maximum associated intensities of VII, 20 km SW of Le Teil (Cornou et al.,
195 2020). Yet, one of the 1873 shocks could be located as close as 5 km south of Le Teil. The BCSF-RéNaSS
196 catalogue (renass.unistra.fr) contains only one earthquake with a magnitude over 4, and two between 3 and 4
197 at less than 60 km from Le Teil in the last decades (since 03/03/1981; Delouis et al., 2019). In 1923, a M_w 3
198 earthquake is located at Le Teil (Manchuel et al., 2018). More recently in 2002-2003, a very shallow (< 200
199 m) earthquake swarm ($M_L < 2$) was detected in the Tricastin area, 20 km SW of Le Teil (Thouvenot et al.,
200 2009).

201 Present-day strain rates estimated by GNSS over the last 10 years are of 1 ± 0.4 nanostrain/yr with a
202 compression trending $\sim N110$, translating into ~ 0.1 mm/yr of shortening over a 100 km long transect (Masson
203 et al., 2019; Delouis et al., 2019) (**Fig. 1a**). In situ stress measurement in Boussenac, 36 km north of Le Teil,
204 indicates a $N140$ maximum horizontal compression (**Fig. 1a**) (Heidbach et al., 2016).

205 As a summary, the Le Teil area is located in a continental intraplate zone where present deformation is
206 slow, but not negligible, and where numerous faults are present. The most preeminent ones strike NE-SW, dip
207 to the SE and are inherited from an Oligocene phase of extension.

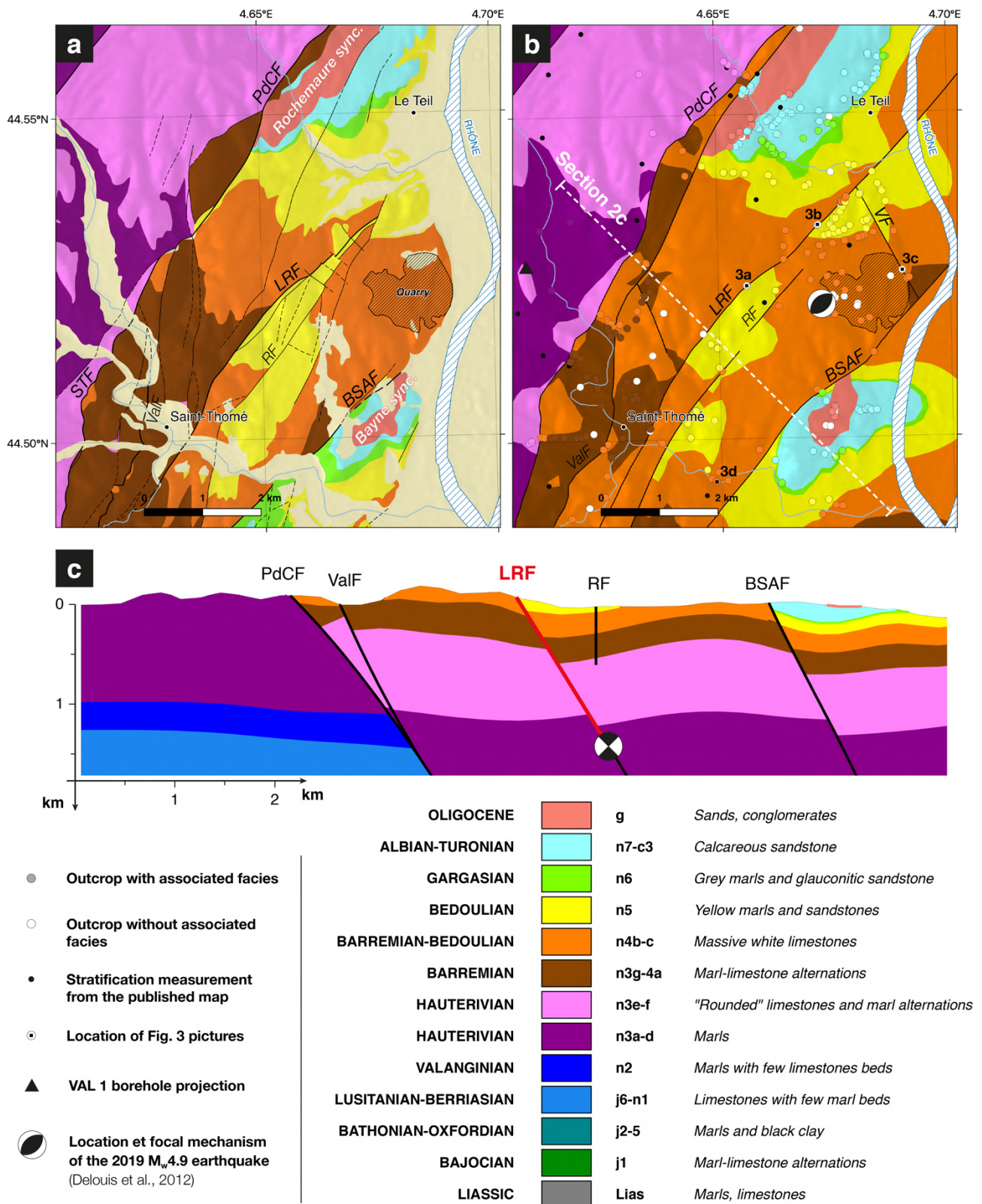


Figure 2. Geological maps and cross-section of the rupture area. (a) Ardèche Geological map (Saint Martin, 2009) with original geological units grouped according to the 3D model stratigraphic pile shown below (see

212 section 3.2 and Fig. S1). Faults' names as defined by Elmi et al. (1996). (b) Surface map of the 3D geological
213 model. Coloured dots indicate location of surface observations used to constrain the 3D model; circled dots
214 labelled 3a to 3d show location of Fig. 3 pictures. The star shows location of the Le Teil earthquake epicenter
215 (Delouis et al., 2021) (c) Geological cross-section across the 3D model, along the trace shown in b. The star
216 shows the projected location of the Le Teil earthquake hypocenter (Delouis et al., 2021) and the red segment
217 of the LRF represents the part that ruptured during the earthquake. *PdCF*: Pontet-de-Couloubre fault; *STF*:
218 Saint-Thomé fault; *ValF*: Valgayette fault ; *LRF*: La Rouvière fault; *RF*: Rocherenard fault ; *VF*: Violette
219 Fault; *BSAF*: Bayne-St-Alban fault.

220 3 Geological 3D model

221 In order to discuss potential relationships between the geological structure and the earthquake rupture,
222 we build a 3D geological model of a 7x10 km area surrounding the surface rupture and the epicenter to a depth
223 of 3 km below sea level. The surface geology of le Teil area was already described on geological maps of
224 Aubenas (Kerrien et al., 1989) and Montélimar (Lorenchet et al., 1979) at the scale of 1:50 000, as well as on
225 the harmonized map of Ardèche (Saint Martin, 2009). However, the design of a 3D geological model requires
226 new fieldwork and the re-definition of geological units.

227

228 3.1 Methods

229 We build a 3D geological model using the GeoModellerTM software. In such a model, layer
230 orientations measured in the field are interpolated to define a potential field that describes the geometry of the
231 corresponding formation (Lajaunie et al., 1997; Calcagno et al., 2008). The base of each formation is an
232 isopotential surface that goes through contact point(s) relative to the underlying formation. The formations
233 parallel to each other are grouped into series. A geometrical relationship must be defined for each series
234 (erosive or onlapping) depending on whether it crosscuts the underlying ones or not (Calcagno et al. 2008).
235 This approach is well adapted to model the geometry of sedimentary series but requires the definition of the
236 series and having as many structural measurements (orientations of the layers) and contact points as possible.
237 Faults are considered as discontinuities in the potential fields. They are defined by their own potential-field,
238 from orientation and location data, and can be set as infinite if they are continuous across the whole model, or
239 finite if they end within the model box. It is necessary to define which formations and other faults are cut by
240 each fault.

241

242 3.2 Stratigraphic pile

243 Most formations outcropping in the model zone are Lower Cretaceous marine sediments including
244 limestones, marls, and marl-limestones alternations. The so-called Urgonian facies (Barremian, lower-Aptian),
245 ubiquitous in the Vocontian basin, corresponds to a more than 200 m thick layer of massive light limestones
246 that are exploited by the cement industry (which includes a historical Lafarge site, active since 1833, and a

247 large active quarry still in operation). Overlying layers are mainly silico-clastic, with sandstones, marls and
248 calcareous sandstones of Upper Aptian, Albian, Cenomanian and Turonian age. That transition is due to a
249 progressive emersion, considered as a far-field effect of the Pyrenean orogenesis, but it is not associated with
250 a major angular unconformity. A main stratigraphic unconformity is present at the base of the Oligocene
251 continental deposits (conglomerates and colored sands).

252 The model stratigraphic pile is built from the stratigraphy described in detail for the 1:50000 Aubenas
253 geological map (Elmi et al., 1996), taking into account the 3D model specificities. Superficial, mostly
254 Quaternary, deposits are not described in the 3D model. According to the geological map, 16 other formations
255 outcrop in the zone. Whilst all these formations have been identified in the field, some of them were merged
256 and only 8 formations appear in the model pile (**Fig. 2; Fig. S1**). Underlying formations do not outcrop in the
257 restricted zone at the surface but appear in the model as 5 distinct formations (**Fig. 2; Fig. S1**). Names given
258 to the new formations do not reflect precise stratigraphic ages. Despite some sedimentation gaps and slight
259 unconformities, all Mesozoic formations have been gathered in the same series, while the Oligocene
260 corresponds to a discordant series.

261

262 **3.3 Fieldwork**

263 During ten days of fieldwork, we collected data at more than 300 locations (**Fig. 2b**). We used these
264 data to build a geological database aimed at standardizing the storage, referencing, and sharing of geological
265 data. Most of these data consists in the determination of the facies and in their attribution to the stratigraphic
266 chart and formations of the 3D model pile, as well as measurements of the strike and dip of the stratification
267 (**Fig. S2**). Other data are defined as contact points at the base of a series or as fault location (**Fig. S2**).

268 One key point of 3D geological modeling is to define the fault network. In the Le Teil area, because
269 of the dense vegetation cover, most faults are defined from the mapping of the sedimentary formations, but
270 some faults may be directly observed in the field. The La Rouvière fault was already mapped previously
271 (Kerrien et al., 1989), and we carefully checked its trace along which fault planes are exposed at four locations
272 (e.g. **Fig. 3a**). While the main fault trace trends N50 on average, local fault planes trend from N5 to N80.
273 Observations of slickensides on fault planes suggest that the more easterly trending planes have a large strike-
274 slip component (**Fig. 3b**). The LRF have locally a clear geomorphic expression (Ritz et al., 2020), and we were

275 able to precisely map its trace between the outcropping planes on a LiDAR Digital Elevation Model (DEM)
276 acquired one week after the earthquake, with a resolution of 25 cm (same data used by Ritz et al., 2020). Both
277 this trace and fault plane measurements collected on the field constrain the geometry of the LRF in the 3D
278 model.

279 About two kilometers west of Le Teil, the Pontet-de-Couloubre fault and the Valgayette fault are 200
280 m apart from each other and bound the Rochemaure Oligocene basin (**Fig. 2b**). The two faults merge further
281 north. Several other NNW-SSE (~N150) strike-slip faults, unreported in previous mapping, are visible in the
282 field, including spectacular fault planes (**Figs 3c, S3b and S4**). Our fault mapping is mostly in agreement with
283 the existing geological maps. Differences arise as only the main faults appear in the 3D model. We also slightly
284 changed the trace of some of them and found some unreported faults (**Fig. 2**). The main faults in the 3D model
285 are NE-SW striking, SE dipping normal faults crossing the whole zone, affecting both the Cretaceous and
286 Oligocene deposits: *Alba*, *Pontet-de-Couloubre* (that was previously considered as two distinct faults: Pontet-
287 de-Couloubre and Saint-Thomé faults), *Valgayette* (with a different trace), *La Rouvière*, and *Bayne-St-Alban*
288 faults (**Fig. 2**). Three other finite faults, as they do not cross the whole area, are also considered in our 3D
289 model: the Rocherenard fault (shorter and subdivided in two branches with respect to previous mapping), and
290 two previously unreported faults trending N150 including the Violette fault.

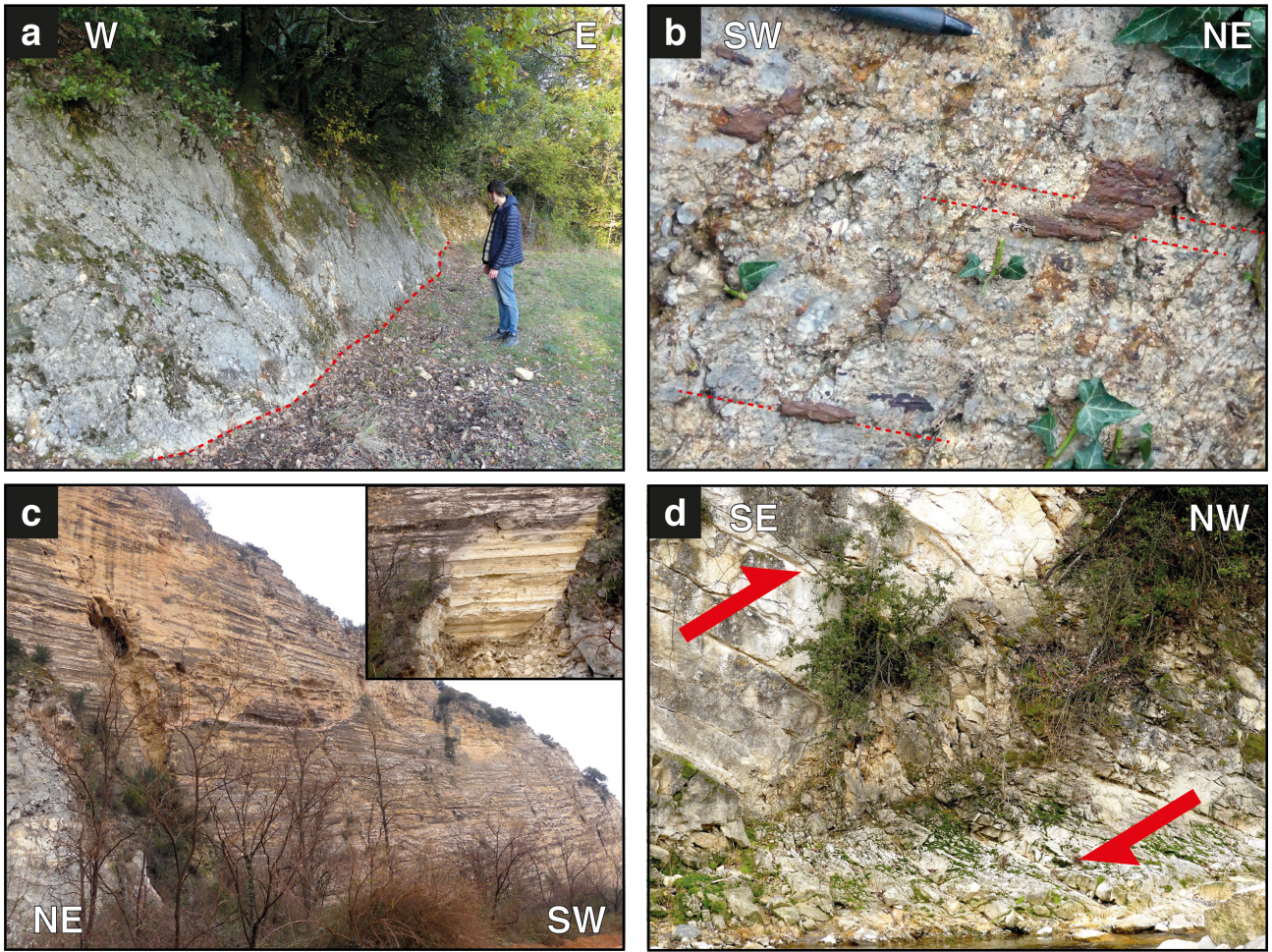


Figure 3. Field observations. (a) [Site LT11] Fault plane striking N45-60°E attributed to La Rouvière Fault (LRF). Neither clear slickensides nor evidence of recent coseismic slip was found on this plane, although it appears collocated with the InSAR-derived rupture (within its location's uncertainties). (b) [Site LT5b] Slickensides (N80-22°) on the LRF fault plane striking N73-72°S. (c) [Site LT122] 200m long, >30m high fault plane striking N150, delimiting an abandoned quarry face in Le Teil cement quarry. This plane displays well-marked slickensides close to horizontal (inset: closer view). (d) [Site LT106] Knee-bend, close to faulting, with a horizontal fold axis trending ~N55. This compression evidence could be associated with the recent Alpine tectonic phase responsible for the Le Teil earthquake. Locations of sites 3a to 3d are shown on Fig. 2.

3.4 Other constraints

We used 15 strike and dip measurements from the Ardèche geological map (Saint Martin, 2009), at locations that we could not explore (**Fig. 2b**, **Fig. S2**), to complement our field data. As the 3D geological model does not assume any formation thickness, it is necessary to dispose of contact points for the formations that do not outcrop. For this purpose, we used the interpreted log of the Valvignère (VAL 1) 4600 m deep borehole (**Fig. S5**) (<http://infoterre.brgm.fr/page/banque-sol-bss>). Although this borehole is located 1 km outside the model box (**Fig. 1b**), the stratification is almost flat in this area. Therefore, we could safely translate it within the box at a location with similar elevation and outcropping formation (**Fig. S2**).

As the dataset remains heterogeneous, with for example few data in the eastern part of the model because of the Quaternary sediments cover in the Rhône valley or in the Le Teil urban area, and with very few constraints at depth, the initial GeoModeller solution barely manages to fit all surface observations. It is thereby necessary to add additional constraints to the model. The methodology is somewhat the same as that followed by a geologist drawing cross-sections at depth from information limited to the surface, making some basic assumptions, such as the continuity of the layers (in the absence of faults) and the approximate conservation of their thicknesses. We hence define ad-hoc additional constraints to the model. The resulting geological map reproduces most of the surface observations (**Fig. 2b**), with some discrepancies considered as negligible. It is worth noting that the 3D geometry of the faults at depth is only defined from field-based measurements.

3.5 Results

The resulting 3D geological model is provided in a 3D PDF format in Supplementary Materials, while 3D views in **Fig. S6**, and 2D views of the model are shown in **Figs 2b, c** and **S7**. The surface map shows the same general pattern as the previous geological maps (Kerrien et al., 1989; Saint Martin, 2009), with the same major faults and the Bayne and Rochemaure syncline folds (**Figs 2** and **S7**). However, they differ by several points. **(1)** The existing maps show necessarily more complexity and details than our simplified model. **(2)** We locally have different interpretations regarding the fault network. For instance, on previous maps, the northern part of the LRF fault is cut by four, possibly dextral, NW-SE faults. We did not detect such faults and, based on the LiDAR DEM and field work, we assume that the fault is continuous. In the same area, we map the Rocherenard fault as discontinuous and not connected to La Rouvière fault to the NE. Conversely, we add in

329 the 3D model two finite faults with a N150 azimuth, because we have clear field evidence of their importance
330 in the local structure (**Figs 3c** and **S4**). We interpret these faults as dextral faults linked to the N-S Pyrenean
331 compression phase. **(3)** Consistent with our field observations, the two syncline folds limbs have significantly
332 lower dips than those depicted on previous geological maps (**Fig. S7**). However, their fold axes are compatible
333 with a post-Oligocene NW-SE compression, associated with the “Rhodanian” deformation phase according to
334 Elmi et al. (1996). At other locations we observed folds with axes compatible with that deformation phase
335 (**Fig. 3d**). These structures are too small to be visible in the 3D model, but out of our mapping zone (South of
336 Bayne syncline), two large NE-SW anticlines are described by Elmi et al. (1996).

337 The geological 3D model allows us to estimate apparent normal offsets of ~1000m and ≥ 150 m for the
338 Pontet-de-Couloubre-Valgayette and Bayne-St-Alban respectively. The offset on the LRF ranges between 100
339 and 200 m.

340 4 InSAR time series analysis

341 The coseismic interferograms produced in the days following the Le Teil earthquake played a key role
342 in guiding the early post-seismic field missions in the earthquake area (Delouis et al., 2019; Cornou et al.,
343 2020). This dataset helped to constrain the location and spatial extent of the surface rupture, guiding further
344 seismological, geodetic and tectonic studies of the earthquake (Mordret et al., 2020, Ritz et al., 2020, De
345 Novellis, 2020, Causse et al., 2021, Vallage et al. 2021).

346 However, past studies of the earthquake involving InSAR data rely on the analysis of only a limited
347 number of individual coseismic interferograms. All were computed from radar images acquired by the ESA's
348 Sentinel-1 satellites a few days before and after the earthquake (Cornou et al., 2020, Ritz et al., 2020, De
349 Novellis, 2020, Vallage et al. 2021). These interferograms were processed and unwrapped using different
350 methodologies and remain affected by atmospheric phase delays and coherence loss. Here we use a time series
351 analysis of Sentinel-1 data acquired every 6 days over a period of about ten months before the earthquake and
352 three months after the earthquake. This approach aims **(1)** to improve the signal-to-noise ratio and refine the
353 coseismic surface displacement field (Grandin et al., 2017, Liu et al, 2021), in particular the surface slip
354 distribution along fault, by mitigating stratified tropospheric phase delays and averaging temporally
355 uncorrelated atmospheric noise (see section 4.1), and **(2)**, given the shallow depth of the earthquake, to
356 investigate potential shallow deformation along the fault during the pre- and post-seismic periods.

357

358 4.1 Data and Methods

359 We derive a time series of surface displacement from Sentinel-1 images acquired in Interferometric
360 Wide Swath mode along one ascending track (relative orbit A059, **Table 1**). We use the complete data archive
361 between 2019/01/04 and 2020/01/29, from sub-swath IW3 only (incidence angle of $\sim 44^\circ$), cropped in an 80
362 by 80 km zone around the earthquake epicenter (**Fig. 1a**). We follow a Small Baseline Subset (SBAS) approach
363 to take advantage of the redundancy on the phase information in a network of interferograms in order to
364 compensate for temporal decorrelation and atmospheric delays (Berardino et al., 2002). Our network of
365 interferograms (**Fig. S8**) includes both short and long temporal baselines, with a maximum timespan of 11
366 months, resulting in 254 interferograms built from 66 images.

367 The interferogram processing and time series inversion are performed using the NSBAS software
368 (Doin et al., 2011), partly derived from ROI_PAC (Rosen et al., 2004) and adapted to Sentinel-1 data for
369 spectral diversity corrections (Grandin, 2015). Orbital and topographic corrections are performed using ESA
370 precise orbits and the Shuttle Radar Topography Mission (SRTM) 1-arc second Digital Elevation Model (Farr
371 et al. 2007). Corrections from stratified tropospheric phase delays are computed using the ERA5 reanalysis
372 data from the European Centre for Medium-Range Weather Forecast (ECMWF) (Doin et al. 2009; Jolivet et
373 al. 2011). Interferograms are multilooked by a factor of 4 in azimuth and 16 in range for unwrapping, leading
374 to a final pixel size of about 80 m. Filtering is made through a weighted average of the phase gradient, based
375 on colinearity (Pinel-Puysegur et al., 2012), in sliding windows of 6 pixels. Unwrapping is performed using
376 the branch-cut algorithm (Goldstein et al., 1988). The coherence threshold used to build masks before
377 unwrapping is adapted depending on the temporal baseline of the interferograms, and on whether the
378 interferogram contains coseismic signal or not. We set the unwrapping to be more restrictive for the long
379 temporal baseline interferograms than for the short baseline ones, in order to avoid unwrapping errors due to
380 temporal decorrelation. For the coseismic interferograms only, a manual cut is also introduced to prevent the
381 unwrapping path from crossing the rupture. The trace of this manual cut (**Fig. 4**) is both consistent with the
382 phase discontinuity visible on the wrapped unfiltered interferograms, with the main surface ruptures we
383 observed on the field, and with the LRF inherited scarp revealed by the LiDAR high-resolution DEM (Ritz et
384 al., 2020). Unwrapped interferograms are first visually checked in order to detect large unwrapping errors.
385 We iteratively compute the time series to recover the phase evolution at each date of acquisition from the
386 unwrapped differential interferograms. Considering a typical SBAS approach, the phase delays of unwrapped
387 interferograms are inverted pixel by pixel to solve for the total phase delay of each date relative to the first
388 date. We apply an additional linear constraint in case sub-networks of interferograms for a pixel could not be
389 connected due to unwrapping issues (Lopez-Quiroz et al., 2009). After a first inversion, we remove the noisiest
390 interferograms from the dataset as well as those presenting large scale unwrapping errors, using a Root Mean
391 Square (RMS) misclosure criterion (pixelwise misclosure within the interferogram network after time series
392 inversion, Lopez-Quiroz et al., 2009). The network thus reduces to 199 interferograms based on 60 images
393 (**Fig. S8**). Residual unwrapping errors are automatically corrected in an iterative procedure during the final
394 NSBAS time series computation, using network adjustment to minimize the RMS misclosure (see RMS

395 misclosure averaged per pixel in **Fig. S9a**).

396 In the following analysis, we mask pixels that are not covered by at least one coseismic interferogram.
397 Indeed, some pixels close to the rupture zone are not necessarily unwrapped on coseismic interferograms due
398 to decorrelation. As the time series inversion is performed for each pixel independently, if a pixel has not been
399 unwrapped in any coseismic interferogram, the pre- and post-event interferograms' sub-networks are disjoint
400 for this pixel. In that case, the algorithm extrapolates the pre-event linear trend to the post-event period (Lopez-
401 Quiroz et al., 2009), leading to potentially incorrect coseismic displacement values at these pixels.
402 In a last step, we perform a temporal decomposition of the unfiltered time series to extract the coseismic
403 displacement (similarly to Grandin et al., 2017) as well as a linear velocity. The LOS displacement at a given
404 pixel d_{LOS} at a time t writes as:

$$405 \quad \quad \quad 406 \quad \quad \quad d_{LOS}(t) = a.t + b.H(t_{cos}) + c \quad (1)$$

407
408 where a is the velocity, b the coseismic offset, H a Heaviside step function, t_{cos} the date of the earthquake, and
409 c an offset parameter to account for atmospheric noise in the first image of the time series (used as reference).
410 We do not include a seasonal term in this decomposition as the relatively short time span of the time series
411 (one year) does not provide enough information to constrain it well. Finally, maps of ground velocity,
412 coseismic displacement and cumulative residual of the decomposition are geocoded for further analysis.

413

414 **4.2 Results**

415 The coseismic LOS displacement map (**Fig. 4a**) displays less noise than single interferograms for the
416 same track, thanks to the time series analysis procedure described above. This coseismic map shows an
417 excellent spatial coverage on the NW side of the earthquake rupture (foot-wall), while higher decorrelation on
418 the hanging-wall leads to slightly worse coverage on the SE side. In the LOS, we observe up to 10 cm of
419 positive displacement (toward satellite) on the hanging-wall and 7 cm of negative motion on the foot-wall
420 (away from satellite), with a maximum relative displacement reaching 16 cm in the SW part of the rupture,
421 close to the location 4.65°E, 44.52°N (**Figs 4a and d**). Other smaller local slip maxima can be noticed in the

422 NE part of the rupture. Our results confirm that the total rupture length is about 5 km (**Fig. 4d**).

423 The green squares in **Fig. 4d** indicate the vertical offsets measured by Ritz et al. (2020) using terrestrial
424 LiDAR, projected in the LOS, so that they are comparable to our InSAR relative displacements (black profile
425 in **Fig. 4d**), assuming that the displacements measured by InSAR are mainly in the vertical direction. Surface
426 displacements measured by LiDAR at sites #1, #2 and #7 are much smaller than the total amount of
427 displacement retrieved by InSAR. This inconsistency is most likely explained by a difference of scale and
428 resolution between the techniques used, since InSAR measures the distributed deformation (at tens of meter
429 scale) while field LiDAR measures more localized deformation (at centimeter scale). This would be consistent
430 with the suggestion by Ritz et al. (2020) that the deformation is more distributed in the north-eastern segment
431 of the rupture. On the contrary, LiDAR measurement #5 indicates a slightly larger displacement than the one
432 estimated by InSAR. This might be explained by the 500 m distance between our two profiles. If the
433 deformation is very localized in this part of the rupture, as suggested by Ritz et al. (2020), the relative
434 displacement between these two InSAR profiles may not capture the maximum of the displacement because
435 they are not close enough to the fault. Therefore, the field measurement could exceed the InSAR measurement
436 there.

437 The linear velocity of the time series decomposition is difficult to interpret (**Fig. 4b**). Given the very
438 low compression rate in the Le Teil region (~ 0.1 mm/year in the $\sim N110$ direction, Masson et al, 2019), this
439 linear term most likely represents the aliased seasonal atmospheric signal, dominating, especially as our time
440 series covers a relatively short time span (one year).

441 After removing the coseismic and linear trend from the unfiltered time series, we analyse the
442 cumulative residual displacement map to detect potential pre-seismic deformation or afterslip. We do not
443 identify (**Fig. 4c**) any clear spatial pattern in the vicinity of the LRF that could be interpreted as pre- or post-
444 earthquake deformation. The cumulative displacement map from post-seismic dates only does not show such
445 pattern either. Thus, we conclude that there was no post-seismic deformation for this earthquake, or at least no
446 *detectable* post-seismic deformation (it might be too small or too deep to be seen with InSAR). It justifies the
447 simple decomposition strategy adopted, into linear and coseismic terms only, without a post-seismic
448 logarithmic term. The analysis of the relative LOS displacement between points located on either side of the
449 Le Teil earthquake rupture only a few hundred meters from each other confirms no relative pre- or post-seismic

450 motion (**Fig. 4e**). Such a relative displacement between points situated at very close distance can be assumed
451 to be little affected by atmospheric noise because spatially correlated noise is largely removed by the double-
452 difference operation. No obvious signal arises in the relative time series associated with these points, although
453 it shows a higher dispersion from May 2019 to the date of the earthquake (0.29 cm and 0.48 cm before and
454 after May, respectively). However, due to the short time-span covered and the lack of a specific spatial pattern
455 near the fault, we interpret this higher dispersion as a residual uncorrelated seasonal signal, possibly of
456 atmospheric or hydrological origin, rather than actual pre-seismic deformation.

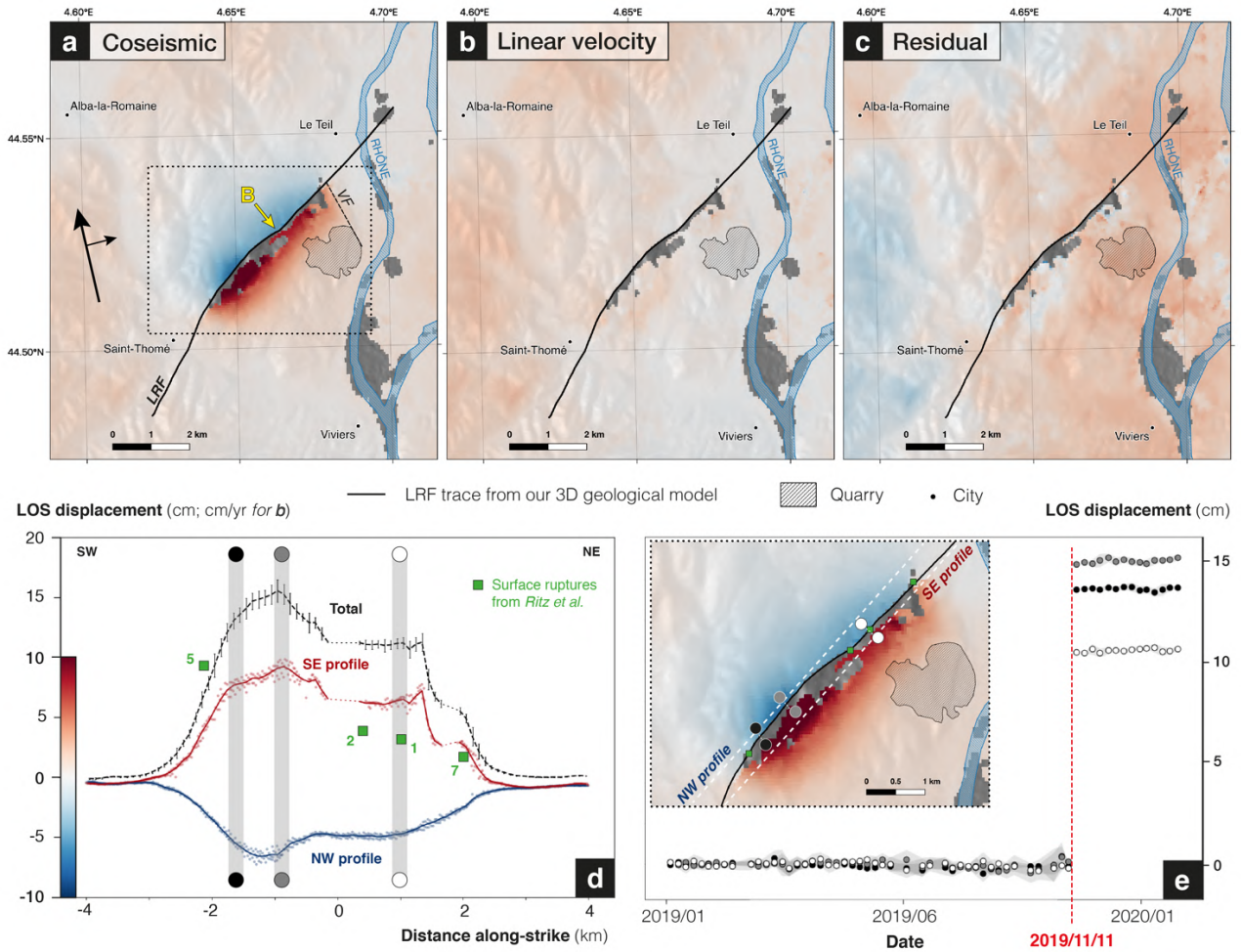


Figure 4. InSAR time series decomposition results (a) Coseismic Line Of Sight (LOS) displacement and (b) linear LOS velocity, best-fitting the InSAR time series over the entire observation time span. (c) Cumulative residual displacement of the InSAR time series decomposition, after removing coseismic signal and cumulative displacement due to linear trend. (d) Along-strike distribution of coseismic LOS displacement. Red (resp. blue) profile shows slip distribution along the southeastern (resp. northwestern) side of the fault; see location of profiles in e. Black profile is the differential between red and blue profiles and represents the total relative displacement along the rupture trace (error bars correspond to the sum of the standard deviations of the two profiles). Green squares are vertical surface displacements (projected on LOS) measured by terrestrial LiDAR from Ritz et al. (2020), with their original numbering. Grey vertical bars indicate along-strike location of sites for which InSAR time series are shown in e. (e) Relative time series for three pairs of points located on each side of the rupture (black, grey, white dots located on inset map from a. 2 sigma envelope of noise level is

shown in light grey. Color code for InSAR maps in a to c and e is shown on vertical axis of d (*in cm for a, c, e; in cm/year for b*). Positive LOS changes indicate motion toward the satellite. The yellow “B” in a indicates a fault bend discussed in section 6.2. *LRF*: La Rouvière Fault; *VF*: Violette Fault.

5 Coseismic slip inversion

We rely on InSAR data as the only geodetic data available to invert for the coseismic slip distribution at depth, using the CSI python library (github.com/jolivet/csi; Jolivet et al., 2015). We use as input the LOS coseismic displacement map extracted from our time series as described in section 4 for track A059, and unwrapped coseismic interferograms for the other three tracks (**Table 1, Figure S11**). These single interferograms were processed following the same workflow and parametrization as described in section 4.1, except for the multilooking factors, which are 2 in azimuth and 8 in range for unwrapping, leading to a final pixel spacing of about 40 m.

Table 1. InSAR dataset used as input for the slip inversion.

Sentinel-1 track	Type of data	Acquisition dates	Final downsampling distance (m)
A059 (ascending)	Coseismic displacement extracted from the time series	Between 2019-01-04 and 2020-01-22	200
A161 (ascending)	Interferogram	2019/11/01-2019/11/13	400
D037 (descending)	Interferogram	2019/11/11-2019/11/17	400
D139 (descending)	Interferogram	2019/11/06-2019/11/12	400

We downsample the four InSAR datasets using a distance-based algorithm in CSI (pixel size decreases as an exponential function of the distance to the fault trace). As we have more confidence in the displacement map derived from our time series, especially in the near-field, we downsample this dataset using a final 200 m resolution (closest to the fault) while using 400 m for interferograms. This leads to a greater number of data

490 points (about 1100), and therefore a greater weight in the inversion for track A059 than for the other three
491 tracks (about 470 data points each). In order to prevent some of the downsampled pixels to cut across the
492 surface trace of the fault, we remove all points within a 180 m buffer in the vicinity of the fault trace. Our
493 dataset still preserves a high level of detail on the near-fault deformation signal enhanced by the time series,
494 helping to constrain the shallow part of the slip distribution.

495 We model surface displacements due to slip on dislocations embedded in a homogeneous elastic half-
496 space. Our fault model is tied to the surface trace of the LRF defined in our 3D geological model derived from
497 field observations and LiDAR analysis and projected onto the free surface of the elastic half-space. From this
498 trace, striking N43 in average, we build a fault plane with a constant dip (the value of which is detailed
499 hereafter) to the South-East, discretized into triangular patches. The patch size is ~150 m at the surface,
500 increasing to ~300 m at the base of the fault (at a depth of around 4 km). We compute the Green's functions
501 relating unit slip on each triangular patch to surface displacements using the method of Meade (2007) for
502 triangular patches. We perform a static inversion using a non-negative least squares strategy (Tarantola, 2005),
503 with the regularization scheme of Radiguet et al. (2011). We account for uncertainties in the InSAR data
504 through the calculation of a data covariance matrix describing the spatial correlation of the pixels (Lohman &
505 Simons, 2005; Sudhaus & Jónsson, 2009; Jolivet et al., 2014; Jolivet et al., 2015).

506 With this setting, we explore the influence of fault dip on the slip distribution for fault planes with
507 dips ranging between 30 and 75°. We compare the different models using a posterior log-likelihood (LLK)
508 function quantifying the misfit associated with each fault geometry (a low LLK indicates smaller misfit).
509 Considering the four InSAR tracks the LLK curves show that a dip between 55° and 60° is favoured by the
510 data, (**Fig. 5a**). This range is consistent with the dips measured on LRF fault planes on the field with an average
511 fault plane striking N44-69°SE (**Fig. 5c**). We use a fixed dip of 57° for the final inversion.

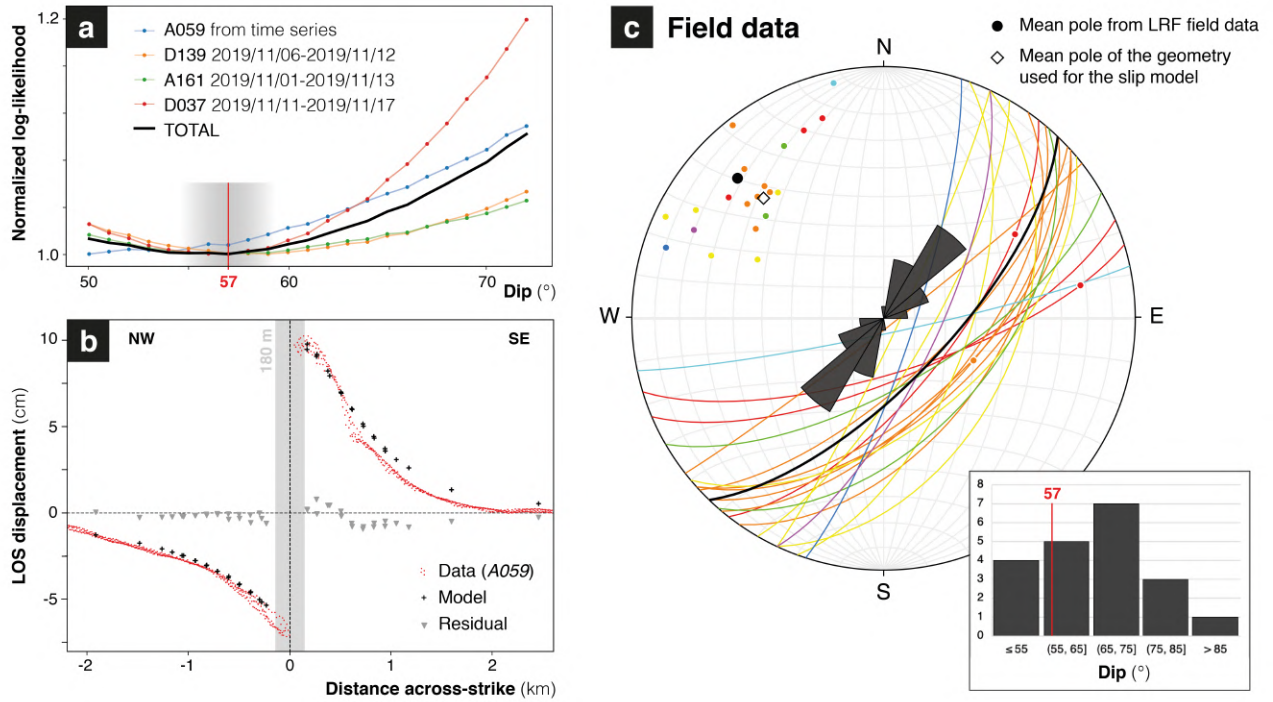


Figure 5. Dip exploration from InSAR analysis and comparison with field data for La Rouvière Fault (LRF)

(a) Dip exploration for InSAR data inversion, based on normalized log-likelihood function. Colors represent different tests made using single coseismic interferograms or coseismic slip map extracted from time series analysis (Fig. 4a). Black curve shows the average function for the whole data set, with best-fitting dips in the range $54\text{--}59^{\circ}$ and a minimum misfit for 57° . (b) Fault-perpendicular LOS coseismic displacement profile (located in Fig. 6d) for A059 track extracted from time series analysis (red dots), compared with corresponding final model profile (black crosses), and model versus data residuals (grey triangles). Data within 180 m from the fault were discarded in the inversion (see text for details). (c) Field observations of LRF planes, shown in a stereonet (equal area, lower hemisphere projection). Each color corresponds to an outcrop. The mean LRF pole (solid black circle; N314-21 $^{\circ}$) and plane (black line) are computed from averaging individual poles and planes of each outcrop. The circles located on lines represent slickenside measurements. The pole of the average fault geometry used for slip inversion from InSAR data (white diamond; N315-33 $^{\circ}$) is shown for comparison. Inset shows dip distribution of the LRF planes measured on the field, compared to the 57° value chosen for the final InSAR data inversion.

529 We then explore the regularization parameters of the inversion, introduced through a model covariance
530 matrix. Three parameters are used in the regularization (Radiguet et al., 2011; Maubant et al. 2020): σ_m a
531 damping value and λ the correlation length, relative to a scaling factor λ_0 , fixed at the minimum interpatch
532 distance (150 m). We optimize the values of σ_m and λ through L-curves analysis (**Fig. S10**), by choosing the
533 best compromise between model roughness (quantified by maximum slip) and the misfit to the data (Radiguet
534 et al., 2011). We use the values $\sigma_m = 0.7$ and $\lambda = 2.5$ km for the final inversion.

535 The LOS surface displacements predicted by our preferred slip model match well the InSAR data (**Fig.**
536 **S11**), with RMS of residual displacements ranging between 0.18 and 0.51 cm. Consistently with its
537 overweighting in the inversion process, the displacement field on track A059 is especially well reproduced
538 with a 0.43 cm RMS misfit (**Fig. 6d**). Our model slightly overestimates the coseismic LOS displacement in
539 the hanging-wall (**Fig. 5b**). After testing several faults dips, we conclude that such feature cannot be fitted with
540 a constant dip geometry, as suggested by the $\sim 5^\circ$ range of equivalent probability dips in **Fig 5a**. Our model
541 though is the best compromise for optimizing the fit to LOS displacement for each track and on both sides of
542 the fault.

543 The resulting slip distribution inverted for the Le Teil earthquake has an equivalent moment magnitude
544 of 4.9, consistent with seismological estimates (Delouis et al., 2019; Cornou et al., 2020; Vallage et al., 2021).
545 The scalar seismic moments are 3.11×10^{16} N.m and 0.9×10^{16} N.m for dip-slip and strike slip, respectively,
546 showing a dominating reverse dip-slip motion (**Figs 6a and b**). This is consistent with the surface InSAR data
547 (**Fig. S11**) displaying a dominance of the vertical motion in the hanging wall (displacement toward satellite
548 for both looking angles) and a dominance of fault-perpendicular horizontal motion in the footwall with respect
549 to vertical motion (opposite signs of motion on ascending and descending tracks). The dip-slip distribution
550 along the fault is characterized by two areas of larger slip: a large one in the SW part of the fault with a
551 maximum slip of 30 cm at 500 m depth and a smaller one in the NE part of the rupture with a maximum dip
552 slip of 24 cm at similar depth. Displacements modelled at the surface have lower amplitudes, with a maximum
553 dip-slip component of 23 cm on the shallowest patches (**Fig. 6a**). The slip profiles along depth (top left inset
554 in **Fig. 6a**) highlight this shallow slip deficit reaching 23% of the maximum slip, which will be discussed later.

555 We performed extensive testing on the strike-slip component of the slip model, which produced very
556 variable distributions and senses of slip. Together with the high dependency of the strike-slip distribution to

557 the setting of the inverse problem (non-negative least square inversion versus bounded inversion for example),
558 this suggests that the strike-slip component is poorly constrained by our dataset. While the best-fitting model
559 that we present here includes a minor (< 9 cm, **Fig. S12**) left-lateral component, we estimate we cannot trust
560 either its distribution, or the sense of the strike-slip motion, and do not discuss them further.

561 To qualitatively assess the robustness of our slip model along fault strike and depth, we compute the
562 sensitivity of the inversion (Loveless & Meade, 2011) (**Figs 6c and S12b**). Note that sensitivity is a purely
563 qualitative indicator (the absolute values actually depend on the number of data we use in the inversion). Only
564 Bayesian approaches could provide a meaningful confidence interval to the estimated slip values. For the dip-
565 slip component, despite small shallow variations due to lack of data close to the fault, sensitivity only decreases
566 significantly below 2 km depth where slip vanishes. We therefore state that our modelled dip-slip distribution
567 is correctly constrained by the data above that depth. Note that the sensitivity for the strike-slip component
568 appears on average about one order of magnitude lower than the dip-slip one (**Fig. S12b**).

569

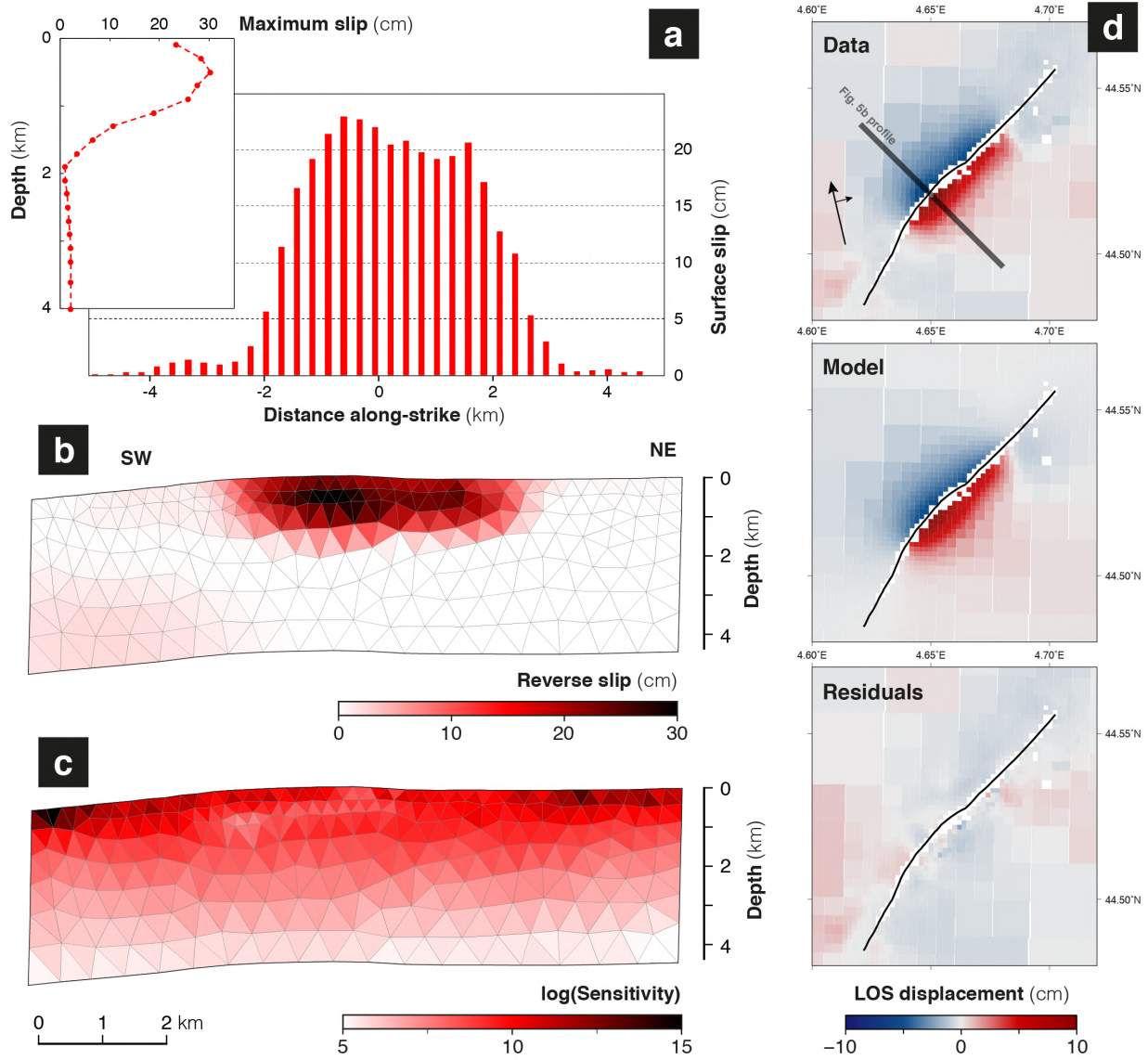


Figure 6. Best slip model. (a) Along-strike distribution of surface slip in our final slip model (dip-slip component only). Inset shows depth distribution of maximum slip. (b) Slip distribution for dip-slip component (strike-slip is shown in Fig. S6). (c) Sensitivity (Loveless & Meade, 2011) of the inversion for the dip-slip component (see Fig. S12 for the strike-slip one). (d) *Top*: downsampled data from time series analysis of A059 track, used for slip inversion; *Middle*: Model; *Bottom*: Residuals.

578 6 Discussion

579 6.1 Reactivation of LRF and rupture geometry

580 Our results, combining 3D geological mapping, InSAR time series analysis and slip inversion suggest
581 a reactivation of the La Rouvière fault during the 2019 Le Teil earthquake. The trace of the LRF defined in
582 our 3D geological model is compatible with the rupture displayed by the InSAR signal. Moreover, although
583 no direct evidence of reactivation was found on the LRF planes, the main evidence of surface rupture
584 associated with the Le Teil earthquake (on which vertical offset could be measured by Ritz et al., 2020) are
585 located very precisely on our trace of LRF (**Fig. S13**). Other evidence was found within several tens to
586 hundreds of meters from the LRF trace, but were less probably directly related to the rupture (e.g. gravitational
587 collapse). Our slip model using a geometry based on the LRF fault trace is able to reproduce InSAR data with
588 a very good level of agreement, reinforcing the consistency of the reactivation hypothesis.

589 Thanks to a time series approach, we improve the coverage of the displacement field extracted from
590 InSAR, compared to interferograms produced just after the earthquake and used in published studies. We show
591 the absence of pre-event deformation or afterslip, while providing, for one Sentinel-1 track, an accurate
592 coseismic LOS displacement map. Although our unwrapping approach is more conservative than in some other
593 works (Ritz et al., 2020; De Novellis et al., 2020), we ensure we can trust all our unwrapped displacements,
594 especially for the highly decorrelating zone in the SW neighbourhood of the rupture. Doing so, we limit the
595 risk of over-interpreting the data.

596 It should be noted that the InSAR displacement map from our times series does not show a multi-
597 segmented rupture, contrary to what has been suggested so far (Ritz et al., 2020; De Novellis et al., 2020).
598 Instead, our data favours a single rupture trace, collocated with the LRF trace. We compared the previously
599 published rupture traces with our coseismic displacement map (**Fig. S13**). The trace from De Novellis et al.
600 (2020) appears to be inconsistent with our data, **(1)** as their main segment is too straight and does not follow
601 the InSAR discontinuity, and **(2)** as our displacement map does not display any evidence for a secondary
602 rupture along La Chade fault. The rupture trace from Ritz et al. (2020) generally follows the surface trace of
603 the LRF that we infer. However, our data are not consistent with secondary ruptures in the NE part of the
604 hanging-wall. As the secondary ruptures presented in these two studies are not mutually consistent, we

speculate that inconsistencies mainly stem from noise in the coseismic interferograms they used, which are mitigated in our time series analysis.

Additionally, our study brings additional constraints on the LRF dip, both at the surface and at depth. Field measurements of LRF planes yield a mean strike of N44 and dip of 70° to the SE (**Fig. 5c**), however associated with a large dispersion (95% confidence interval about $\pm 17^\circ$). The inversion of the InSAR data reveals a best fitting dip in the range 55-60° (**Fig. 5a**). Considering the uncertainty on these estimates, we argue that the LRF should not show substantial variations of dip angle in the depth range ruptured by the Le Teil earthquake (< 2 km), although we cannot exclude a slight steepening close to the surface. De Novellis et al. (2020) used a 52° dip on the LRF for their two faults slip model, and a 62° dip for their single fault geometry, consistent with our modeling results. Vallage et al. (2021) find best fitting dips for a single fault of 60° using InSAR, still in agreement with our estimates. Regarding seismological estimations of the focal mechanism, Vallage et al. (2021) propose a nodal plane striking N45-65°SE, while Delouis et al. (2021) propose nodal planes striking N45 to N65 and dipping 40 to 60°E from waveform inversion. They are all consistent with our results and also suggest that the LRF has a similar dip from the surface to at least 1-1.5 km depth, where the earthquake likely nucleated.

6.2 Potential interactions between 3D geology, fault geometry and earthquake slip

The implementation of a local 3D geological model, combined with the slip model derived from InSAR offers the opportunity to study potential interactions between the earthquake slip and the pre-existing three-dimensional geological structure. The more recent relocations of the point source of the Le Teil earthquake by Delouis et al. (2021) can be discussed together with our slip distribution. The epicentral area that they estimate is located between the western part of Le Teil quarry and the LRF (**Fig. 1a; Fig. 2b**), with a source depth between 1 and 2 km (**Fig. 2c; Fig. 7**; Delouis et al., 2021). It is consistent with our estimate of the fault location and dip.

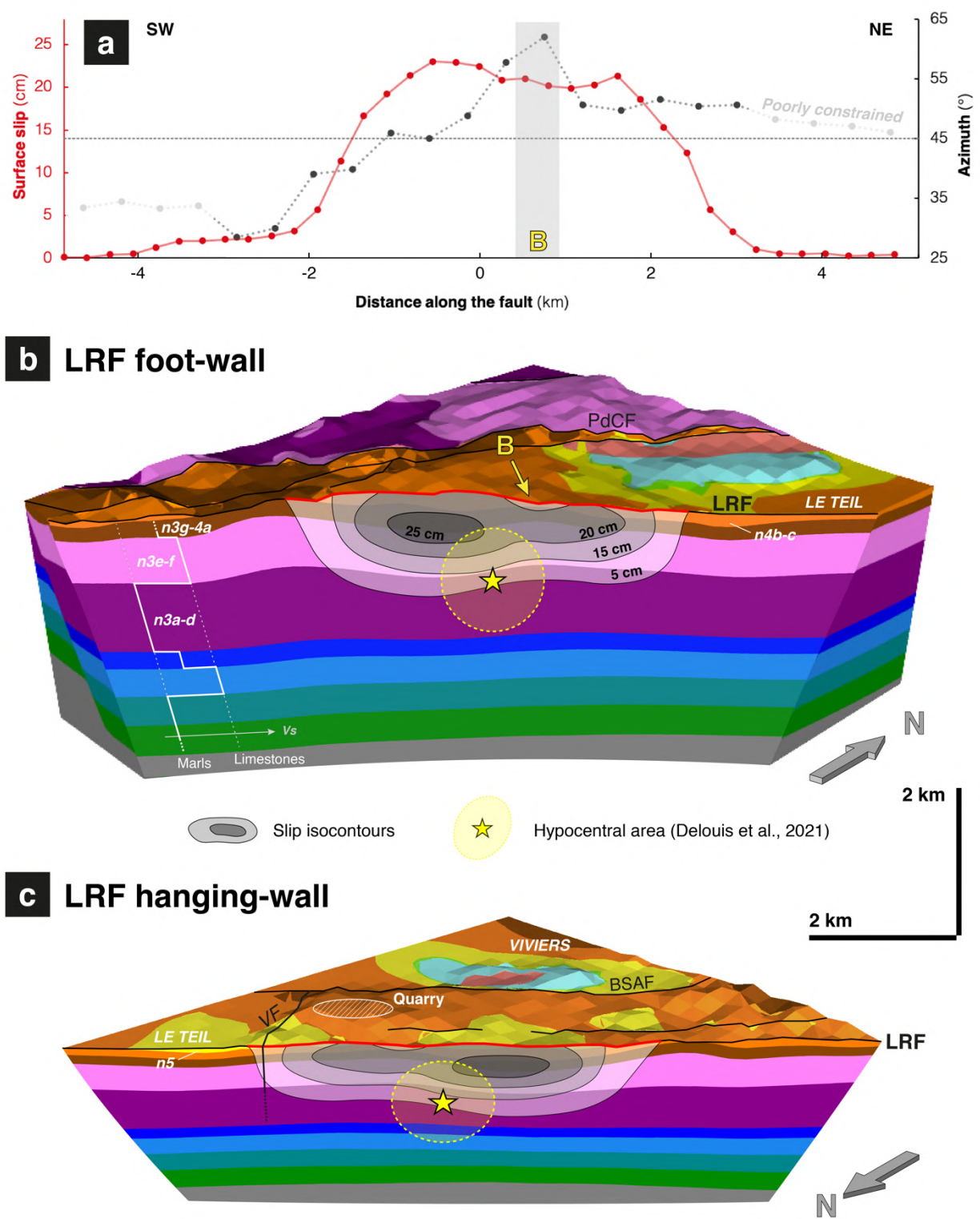
Our fieldwork allows us to map a previously unknown fault, displaying post-Cretaceous strike-slip motion (**Fig. 3c**), with a N150 orientation, that we named Violette fault (VF). In the field, we found no evidence of any fault north of its inferred crossing point with the LRF. We therefore map the VF fault stopping on the LRF fault, assuming that the LRF is more recent. Our InSAR coseismic displacement map shows that the uplift

633 of the hanging-wall vanishes to the NE in the area where the VF intersects the LRF (**Fig. 4a**). Consistently,
634 our modeled slip on fault tapers down to zero to the NE in the interaction zone between the VF and LRF (**Fig.**
635 **7c**). We speculate that the connection area of the two faults could have acted as a barrier to the north-eastward
636 propagation of the earthquake, as already documented for other cases in literature (e.g. Klinger et al., 2006;
637 Walters et al., 2018).

638 The combination of our 3D geological model and the slip model also allows one to study potential
639 geological constraints on the depth extension of slip during the earthquake. As mentioned earlier, the Le Teil
640 earthquake is very shallow, and slip does not exceed 25% of its maximum value (i.e. slip < 8 cm) at depths
641 larger than 1.5 km (**Fig. 6a**). Our 3D geological model shows a lithological transition at ~1 km depth (± 100
642 m between the foot-wall and the hanging-wall of the LRF) between massive limestone units (n3e-f) on the top
643 and an underlying thick (~1 km) marl unit (n3a-d) (**Figs 7b and c**). This transition is likely associated with a
644 downdip drop of rock rigidity along the LRF plane. This feature was previously noticed in local velocity
645 models (Causse et al., 2021), by the need to introduce a low-velocity zone about 1 km thick at depths greater
646 than 1200 m. Earthquake propagation is known to be facilitated in high rigidity media. Specifically, in a region
647 where geological units are similar to those observed in Le Teil region, Gratier et al. (2013) showed that
648 limestones' layers favour seismic slip while marls often creep. Thus, our results suggest that while most of slip
649 occurred in massive limestones (n3e-f and n4b-c, i.e. the Urgonian limestones), the n3a-d marls layer could
650 have prevented the earthquake nucleation and/or propagation at greater depth.

651 According to our slip model, the coseismic slip reached the surface along the whole rupture length
652 (~5km), but with heterogeneous amounts of surface slip. Two main slip maxima can be identified in the surface
653 slip distribution (**Figs 6a and 7a**), corresponding to the two main slip patches of the slip distribution at depth.
654 A significative change in the LRF strike, marked by a peak at N60, is observed in between these two maximum
655 slip locations and is marked "B" in **Figs 4a, 7a and 7b**. This change in azimuth is well resolved since the
656 central portion of the LRF was mapped using a 25cm LiDAR DEM and complemented by field measurements
657 (while the SW and NE parts of the LRF — greyish in **Fig. 7a** — were only constrained by a few outcrops).
658 Such type of geometrical complexity may act as barrier to earthquake rupture propagation (King & Nabelek,
659 1985; Wesnousky et al., 2006; Klinger, 2006). Hence, we suggest that this change in the LRF surface geometry
660 could have restrained the slip propagation. We have no constraints on the potential downdip continuation of

661 this relay zone. However, considering the shallowness of the slip distribution, its impact could remain
 662 significant at depth, and maybe have contributed to the delimitation of the two slip maxima.



663
 664 **Figure 7.** 3D summary of Le Teil earthquake rupture characteristics. (a) Along-strike coseismic surface slip
 665 distribution derived from our model (in red, dip-slip component only) compared to along-strike variations of

666 local fault azimuth (in grey). Poorly constrained azimuths due to limited LRF field evidences are plotted in
667 lighter grey. The yellow “B” letter shows the main bend mentioned in the text. (b) and (c) 3D views of the NW
668 (b) and SE (c) part of our 3D geological model, cut along the LRF fault plane. The detailed lithological
669 description is in Fig. 2. A qualitative velocity model, assumed to represent the variability of rigidities of rocks
670 observed in the field is plotted in b (left side). The isocontours of the slip distribution inferred from InSAR are
671 superimposed in grey, together with hypocentral area (in yellow) from seismological data (preferred relocation
672 of the mainshock by Delouis et al., 2021, with associated uncertainty of ~500 m). *PdCF*: Pontet-de-Couloubre-
673 Fault; *LFR*: La Rouvière Fault; *VF*: Violette Fault; *BSAF*: Bayne-St-Alban Fault.

674 **6.3 A singular earthquake**

675 The characteristics of this earthquake make it out of range in the Wells & Coppersmith (1994)
676 empirical relationships. According to these scaling laws, a 5 km surface rupture length is usually associated
677 with a M_w 5.8-6.1 event, and a 30 cm maximum displacement should result in a M_w 6.3-6.5 earthquake. The
678 Le Teil earthquake does not fit either the updated relationships from Leonard (2010) between rupture length
679 and seismic moment. However, these relationships are not necessarily suited for very small and shallow events,
680 for which small scale variations of physical parameters of the crust could play a critical role (e.g. 2010 M_w 4.9
681 Pisayambo earthquake, Champenois et al., 2017).

682 The shallow slip deficit displayed by our model is also present in the InSAR-derived slip models from
683 previous studies (Delouis et al., 2019; De Novellis et al., 2020; Vallage et al., 2021). In the framework of a
684 homogeneous elastic half-space inversion, it is difficult to assess whether Surface Slip Deficit (SSD; Fialko et
685 al., 2005) is a real feature or an artifact resulting from the lack of data coverage close to the fault, or caused by
686 neglecting the likely complexities of the elastic medium (Xu et al., 2016; Marchandon et al., 2021). Slip
687 modeling is probably more sensitive to these parameters for such a small event than for larger events, for which
688 the spatial resolution is often decreased for the sake of computational tractability. Taking advantage of the 3D
689 geological model built in this study to create a layered 2D, or even 3D, elastic model, and use it to compute
690 the Green's functions, although technically feasible, is beyond the scope of the present study. This would
691 require a way to quantify the physical parameters of the rocks from the different geological facies we observed
692 in the field. This could be achieved through lab experiments on samples or the comparison of the 3D geology
693 with a local velocity model derived from seismological observations. A good resolution in the very shallow
694 part (depth <500m) of such an elastic model would be needed to improve tangibly the fit of the surface
695 displacements.

696 The Le Teil earthquake occurred on an ancient normal fault, for which we observe no evidence of
697 post-Oligocene activity. As suggested by Ritz et al. (2020), although the LRF has a clear geomorphic
698 expression, it is not sharp enough to result from a significant seismic activity in the last tens of thousands of
699 years. An ongoing work by Ritz et al. (2021) suggests from paleoseismological trenches that the LRF could
700 have hosted at least one event in the historical period, with kinematic features consistent with reverse motion.
701 Pending the outcome of these paleoseismological results to come up, based only on geomorphology, we cannot

702 know how recent the first reactivation of the LRF as reverse fault since Oligocene is, as the very slow
703 deformation relative to the erosion rates likely hinders the preservation of this recent activity.

704 Why this earthquake occurred on the LRF, when it is not the fault displaying the largest cumulative
705 offset in the area according to our 3D geological model, is still a matter to debate. Actually, fieldwork and 3D
706 geological modeling have not given us any argument to explain the occurrence of an earthquake on the LRF
707 rather than on any other. The very shallow depth of the event and the small number of aftershocks (Cornou et
708 al, 2020), coupled with the presence of a large active quarry in the LRF hanging wall have led some to propose
709 that the earthquake was induced by a reduction of normal stress along the LRF due to the artificial discharge
710 (De Novellis et al. 2020). This hypothesis has led to a national and international public media debate raising
711 major issues of liability and seismic risk. It has been discussed by a national scientific commission (Delouis et
712 al., 2019) and scientific publications (Ampuero et al., 2020, De Novellis et al. 2020), but no definite answer
713 has yet been reached. Our study did not focus on this aspect, and we found no element which could help in the
714 debate. InSAR time series shows no localized deformation that could be associated with the quarry discharge.
715 Tracking such a signal, if it exists, would probably necessitate to study a much longer InSAR time series.

716 The geological and structural framework in which the 2019 Le Teil event occurred, characterized by
717 NE-SW oriented faults cutting limestones and marls units, is quite ubiquitous along the right-bank of the Rhône
718 river between latitudes 44.3 and 44.8°N (**Fig. 1a**). Moreover, many other smaller quarries exploit the Urgonian
719 limestones in this region. The assessment of the seismic potential of the many faults similar to the LRF,
720 potentially in relation with quarrying activities, is of paramount importance, given the presence of two nuclear
721 power plants located 15 km north and 25 km south of Le Teil. Future studies combining 3D geology, sub-
722 surface imaging and paleo-seismology should help improve the knowledge of faults' activity in this slowly
723 deforming region. Furthermore, the integration of geological datasets at regional scale, together with
724 seismological observations could benefit to seismic hazard assessment, for example through the identification
725 of geological units associated with a higher probability of seismic slip (such as the Urgonian limestone layer,
726 e.g. Thouvenot et al. 2009).

727

728 7 Conclusion

729 The 2019 M_w 4.9 Le Teil earthquake, while not causing heavy fatality, reveals a critical lack of
730 knowledge regarding the activity of the northeastern part of the Cévennes fault system, emphasized by a high
731 vulnerability due to the proximity to nuclear facilities and populated areas.

732 Our study helps characterize the Le Teil earthquake through a multidisciplinary approach. The 3D
733 geological modeling that we carried out provides an updated view of the local geological and structural context
734 in which this event occurred. Our InSAR work enhances the coseismic displacement map proposed previously
735 from single interferograms, and rules out the existence of a significant deformation in the 10 months before
736 and 3 months after the event. The inversion of InSAR data for slip distribution reveals the consistency between
737 InSAR observations and the modeled 3D geometry of the Oligocene La Rouvière fault. The slip model shows
738 almost purely reverse faulting along a single ~ 5 km long rupture, with two main slip patches reaching 30 cm
739 and 24 cm of slip, respectively, at 500m depth, and a fault dip of 55-60°. The rupture ends at the intersection
740 between the La Rouvière fault and the previously unmapped Violette fault which may have acted as a barrier.
741 Our analysis also suggests that both a fault bend and rigidity contrasts in the local stratigraphy influenced the
742 slip distribution. These results confirm that the area is currently undergoing a WNW-ESE shortening which,
743 whilst slow, could reactivate older faults inducing damaging seismicity, and therefore calls for a reassessment
744 of the seismic hazard.

745

746 Acknowledgements

747 This work has been supported by the CNRS-INSU and LGL-TPE. RJ has received funding from the European
748 Research Council (ERC) under the European Union's Horizon 2020 Research and Innovation Programme
749 (Grant Agreement: 758210—Geo4D) and from the Institut Universitaire de France. We acknowledge the
750 constructive reviews of two anonymous reviewers and the Editor H. Yao.

751

752

753

754 Data availability

755 Sentinel-1 data are available online through PEPS (<https://peps.cnes.fr>) or Copernicus
756 (<https://scihub.copernicus.eu>) platforms. Precise orbits were downloaded from European Space Agency's
757 Sentinel-1 website (<https://qc.sentinel1.eo.esa.int/>, in March 2020). SRTM data are provided on Earthdata
758 portal (<https://earthdata.nasa.gov>). ECMWF ERA5 data are available at <https://www.ecmwf.int>.
759 The database of geological observations (DataGeol) generated during this study is available at
760 <https://zenodo.org/record/4836308#.YLDijDYzYWp>. The 3D geological model can be downloaded at
761 https://zenodo.org/record/5974794#.Yf_USC_pUI. The principal maps extracted from the InSAR time series
762 analysis can be downloaded at <https://zenodo.org/record/4836335#.YLDokS8isWo>.

763

764

765 Authors contribution

766 P.H.L. and C.L. conceived the study. L.M. and P.H.L. did fieldwork. L.M. and S.C. did geological 3D
767 modeling. L.M. and C.L. processed and analyzed the InSAR time series. L.M., R.J. and C.L. carried inversion
768 of slip distribution. R.G. and O.C. contributed to InSAR processing. L.A. provided the LiDAR data and
769 contributed to its analysis. L.M., P.H. L., C.L., R.J., R.G. and M.M. contributed to the interpretation and
770 discussion of the results, and writing the manuscript.

771 References

- 772 Ambert, P., Philip, H. & Ritz, J. (1998) Commentaires à la note de R. Lacassin, B. Meyer, L.
 773 Benedetti, R. Armijo et P. Tapponnier. 'Signature morphologique de l'activité de la faille des
 774 Cevennes (Languedoc, France)'. *Comptes Rendus de l'Académie des Sciences Series IIA Earth and*
 775 *Planetary Science*, **12**, 857–859.
- 776 Ampuero, J.-P., Billant, J., Brenguier, F., Cavalié, O., Courboux, F., Deschamps, A., Delouis, B.,
 777 *et al.* (2020) The November 11 2019 Le Teil, France M5 earthquake: a triggered event in nuclear
 778 country, Presented at the EGU General Assembly 2020, EGU. doi:[10.5194/egusphere-egu2020-](https://doi.org/10.5194/egusphere-egu2020-18295)
 779 [18295](https://doi.org/10.5194/egusphere-egu2020-18295)
- 780 Arène, J., Berger, G., Gras, H., Poidevin, J. & Sauvel, C. (1978) Carte géologique de la France au
 781 1/50000, feuille Alès (912), Bureau de Recherches Géologiques et Minières.
- 782 Arthaud, F. & Matte, Ph. (1975) Les décrochements tardi-hercyniens du sud-ouest de l'europe.
 783 Géométrie et essai de reconstitution des conditions de la déformation. *Tectonophysics*, **25**, 139–171.
 784 doi:[10.1016/0040-1951\(75\)90014-1](https://doi.org/10.1016/0040-1951(75)90014-1)
- 785 Arthaud, F. & Seguret, M. (1981) Les structures pyreneennes du Languedoc et du Golfe du Lion
 786 (Sud de la France). *Bulletin de la Société Géologique de France*, **S7-XXIII**, 51–63.
 787 doi:[10.2113/gssgfbull.S7-XXIII.1.51](https://doi.org/10.2113/gssgfbull.S7-XXIII.1.51)
- 788 Arthaud, F. & Laurent, P. (1995) Contraintes, déformation et déplacement dans l'avant-pays Nord-
 789 pyrénéen du Languedoc méditerranéen. *Geodinamica Acta*, **8**, 142–157.
 790 doi:[10.1080/09853111.1995.11105386](https://doi.org/10.1080/09853111.1995.11105386)
- 791 Bandet, Y., Donville, B. & Gourinard, Y. (1974) Premières datations potassium argon du Coiron
 792 (Ardèche, France). *C.R. de l'Académie des Sciences de Paris*, **279**, 2869–2872.
- 793 Barbarand, J., Lucazeau, F., Pagel, M. & Séranne, M. (2001) Burial and exhumation history of the
 794 south-eastern Massif Central (France) constrained by apatite fission-track thermochronology.
 795 *Tectonophysics*, **335**, 275–290. doi:[10.1016/S0040-1951\(01\)00069-5](https://doi.org/10.1016/S0040-1951(01)00069-5)
- 796 Berardino, P., Fornaro, G., Lanari, R. & Sansosti, E. (2002) A new algorithm for surface
 797 deformation monitoring based on small baseline differential SAR interferograms. *IEEE Trans.*
 798 *Geosci. Remote Sensing*, **40**, 2375–2383. doi:[10.1109/TGRS.2002.803792](https://doi.org/10.1109/TGRS.2002.803792)
- 799 Bergerat, F. & Martin, P. (1993) Mise en évidence d'une tectonique distensive synsédimentaire et
 800 caractérisation du champ de contraintes au Trias inférieur-moyen sur la bordure vivaro-cévenole du
 801 Bassin du Sud-Est de la France: la région de Largentière et le forage Balazuc-1 (programme
 802 Géologie Profonde de la France). *Comptes rendus de l'Académie des sciences. Série 2, Mécanique,*
 803 *Physique, Chimie, Sciences de l'univers, Sciences de la Terre*, **316**, 1279–1286.
- 804 Bergerat, F. & Martin, P. (1994) Analyse des failles du forage Balazuc-1 (programme GPF) et
 805 reconstitution des paleo-états de contrainte sur la bordure vivaro-cévenole du bassin du sud-est de la
 806 France; relations avec la marge européenne de la Tethys ligurienne. *Bulletin de la Société Géologique*
 807 *de France*, **165**, 307–315.
- 808 Bergerat, Françoise. (1987) Stress fields in the European platform at the time of Africa-Eurasia
 809 collision. *Tectonics*, **6**, 99–132. doi:[10.1029/TC006i002p00099](https://doi.org/10.1029/TC006i002p00099)
- 810 Blés, J.L., Bonijoly, D., Castaing, C. & Gros, Y. (1989) Successive post-Variscan stress fields in
 811 the French Massif Central and its borders (Western European plate): comparison with geodynamic
 812 data. *Tectonophysics*, **169**, 79–111. doi:[10.1016/0040-1951\(89\)90185-6](https://doi.org/10.1016/0040-1951(89)90185-6)

813 Blès, J.L. & Gros, Y. (1991) Stress field changes in the Rhone Valley from the Miocene to the
814 present. *Tectonophysics*, **194**, 265–277. doi:[10.1016/0040-1951\(91\)90264-S](https://doi.org/10.1016/0040-1951(91)90264-S)

815 Bodeur, Y. (1976) Evaluation de l’amplitude du décrochement cévenol par le décalage des facies
816 récifaux portlandiens des environs de Ganges (Hérault). *Comptes Rendus de l’Académie des*
817 *Sciences-Series II*.

818 Bonijoly, D., Perrin, J., Roure, F., Bergerat, F., Courel, L., Elmi, S. & Mignot, A. (1996) The
819 Ardèche palaeomargin of the South-East Basin of France: Mesozoic evolution of a part of the
820 Tethyan continental margin (Géologie Profonde de la France programme). *Marine and Petroleum*
821 *Geology*, **13**, 607–623. doi:[10.1016/0264-8172\(95\)00075-5](https://doi.org/10.1016/0264-8172(95)00075-5)

822 Calcagno, P., Chilès, J.P., Courrioux, G. & Guillen, A. (2008) Geological modelling from field data
823 and geological knowledge. *Physics of the Earth and Planetary Interiors*, **171**, 147–157.
824 doi:[10.1016/j.pepi.2008.06.013](https://doi.org/10.1016/j.pepi.2008.06.013)

825 Carbon, D., Combres, P., Cushing, M. & Granier, T. (1993) Enregistrement d’un paléoséisme dans
826 des sédiments du pléistocène supérieur dans la vallée du Rhône: quantification de la déformation.
827 *Géologie alpine*, **69**, 33–48.

828 Causse, M., Cornou, C., Maufroy, E., Grasso, J.-R., Baillet, L. & El Haber, E. (2021) Exceptional
829 ground motion during the shallow Mw 4.9 2019 Le Teil earthquake, France. *Commun Earth*
830 *Environ*, **2**, 14. doi:[10.1038/s43247-020-00089-0](https://doi.org/10.1038/s43247-020-00089-0)

831 Champenois, J., Baize, S., Vallee, M., Jomard, H., Alvarado, A., Espin, P., Ekström, G., *et al.*
832 (2017) Evidences of Surface Rupture Associated With a Low-Magnitude (Mw 5.0) Shallow
833 Earthquake in the Ecuadorian Andes. *J. Geophys. Res. Solid Earth*, **122**, 8446–8458.
834 doi:[10.1002/2017JB013928](https://doi.org/10.1002/2017JB013928)

835 Chantraine, J., Autran, A. & Cavelier, C. (1996) Carte Géologique de la France au 1/1000000,
836 Bureau de Recherches Géologiques et Minières.

837 Chardon, D., Aretz, M. & Roques, D. (2020) Reappraisal of Variscan tectonics in the southern
838 French Massif Central. *Tectonophysics*, **787**, 228477. doi:[10.1016/j.tecto.2020.228477](https://doi.org/10.1016/j.tecto.2020.228477)

839 Choi, J.-H., Klinger, Y., Ferry, M., Ritz, J.-F., Kurtz, R., Rizza, M., Bollinger, L., *et al.* (2018)
840 Geologic Inheritance and Earthquake Rupture Processes: The 1905 $M \geq 8$ Tsetserleg-Bulnay Strike-
841 Slip Earthquake Sequence, Mongolia. *J. Geophys. Res. Solid Earth*, **123**, 1925–1953.
842 doi:[10.1002/2017JB013962](https://doi.org/10.1002/2017JB013962)

843 Cornou, C., Ampuero, J.-P., Aubert, C., Audin, L., Baize, S., Billant, J., Brenguier, F., *et al.* (2021)
844 Rapid response to the Mw 4.9 earthquake of November 11, 2019 in Le Teil, Lower Rhône Valley,
845 France. *Comptes Rendus. Géoscience*, **353**, 1–23. doi:[10.5802/crgeos.30](https://doi.org/10.5802/crgeos.30)

846 Delouis B., Ampuero J-P, Audin L., Bernard P., Brenguier F., Grandin R., Jolivet R., Leloup P. H.,
847 Ritz J., Vergne J., Vernant P., Voisin C. Rapport d’évaluation du groupe de travail (GT) CNRS-
848 INSU sur le séisme du Teil du 11 novembre 2019 et ses causes possibles (in french), CNRS-INSU.
849 11 Décembre 2019. [http://www.cnrs.fr/sites/default/files/press_info/2019-](http://www.cnrs.fr/sites/default/files/press_info/2019-12/Rapport_GT_Teil_phase1_final_171219_v3.pdf)
850 [12/Rapport_GT_Teil_phase1_final_171219_v3.pdf](http://www.cnrs.fr/sites/default/files/press_info/2019-12/Rapport_GT_Teil_phase1_final_171219_v3.pdf)

851 Delouis, B., Oral, E., Menager, M., Ampuero, J.-P., Guilhem Trilla, A., Régnier, M. & Deschamps,
852 A. (2021) Constraining the point source parameters of the 11 November 2019 Mw 4.9 Le Teil
853 earthquake using multiple relocation approaches, first motion and full waveform inversions.
854 *Comptes Rendus. Géoscience*, **353**, 1–24. doi:[10.5802/crgeos.78](https://doi.org/10.5802/crgeos.78)

855 De Novellis, V., Convertito, V., Valkaniotis, S., Casu, F., Lanari, R., Monterroso Tobar, M.F. &
856 Pino, N.A. (2020) Coincident locations of rupture nucleation during the 2019 Le Teil earthquake,
857 France and maximum stress change from local cement quarrying. *Commun Earth Environ*, **1**, 20.
858 doi:[10.1038/s43247-020-00021-6](https://doi.org/10.1038/s43247-020-00021-6)

859 Deville, E., Blanc, E., Tardy, M., Beck, C., Cousin, M. & Ménard, G. (1994) Thrust Propagation
860 and Syntectonic Sedimentation in the Savoy Tertiary Molasse Basin (Alpine Foreland). in
861 *Hydrocarbon and Petroleum Geology of France* ed. Mascle, A., pp. 269–280, Berlin, Heidelberg:
862 Springer Berlin Heidelberg. doi:[10.1007/978-3-642-78849-9_19](https://doi.org/10.1007/978-3-642-78849-9_19)

863 Dèzes, P., Schmid, S.M. & Ziegler, P.A. (2004) Evolution of the European Cenozoic Rift System:
864 interaction of the Alpine and Pyrenean orogens with their foreland lithosphere. *Tectonophysics*,
865 **389**, 1–33. doi:[10.1016/j.tecto.2004.06.011](https://doi.org/10.1016/j.tecto.2004.06.011)

866 Doin, Marie-Pierre, Guillaso, S., Jolivet, R., Lasserre, C., Lodge, F., Ducret, G. & Grandin, R.
867 (2011) Presentation of the small baseline NSBAS processing chain on a case example: the Etna
868 deformation monitoring from 2003 to 2010 using Envisat data, pp. 3434–3437, Presented at the
869 Proceedings of the Fringe symposium, ESA SP-697, Frascati, Italy.

870 Doin, M.-P., Lasserre, C., Peltzer, G., Cavalié, O. & Doubre, C. (2009) Corrections of stratified
871 tropospheric delays in SAR interferometry: Validation with global atmospheric models. *Journal of*
872 *Applied Geophysics*, **69**, 35–50. doi:[10.1016/j.jappgeo.2009.03.010](https://doi.org/10.1016/j.jappgeo.2009.03.010)

873 Elmi, S. (1983) La structure du Sud-Est de la France: une approche à partir de la bordure vivaro-
874 cévenole du Massif Central. *Comptes Rendus de l'Académie des Sciences-Series II*, 1615–1620.

875 Elmi, S., Busnardo, R., Clavel, B., Kerrien, Y., Camus, G., Kieffer, G., Bérard, G., *et al.* (1996)
876 Notice explicative. Carte géologique de la France au 1/50000, feuille Aubenas (865), p. 170, Bureau
877 de Recherches Géologiques et Minières.

878 Farr, T.G., Rosen, P.A., Caro, E., Crippen, R., Duren, R., Hensley, S., Kobrick, M., *et al.* (2007)
879 The Shuttle Radar Topography Mission. *Rev. Geophys.*, **45**, RG2004. doi:[10.1029/2005RG000183](https://doi.org/10.1029/2005RG000183)

880 Feraud, G. (1979) Age et mise en place du volcanisme du massif du Coiron (Ardèche, France). *C.R*
881 *Académie des Sciences de Paris*, **289**.

882 Feraud, Gilbert & Campredon, R. (1983) Geochronological and structural study of tertiary and
883 quaternary dikes in southern france and sardinia: An example of the utilization of dike swarms as
884 paleostress indicators. *Tectonophysics*, **98**, 297–325. doi:[10.1016/0040-1951\(83\)90299-8](https://doi.org/10.1016/0040-1951(83)90299-8)

885 Fialko, Y., Sandwell, D., Simons, M. & Rosen, P. (2005) Three-dimensional deformation caused by
886 the Bam, Iran, earthquake and the origin of shallow slip deficit. *Nature*, **435**, 295–299.
887 doi:[10.1038/nature03425](https://doi.org/10.1038/nature03425)

888 Ford, M. & Lickorish, W.H. (2004) Foreland basin evolution around the western Alpine Arc.
889 *Geological Society, London, Special Publications*, **221**, 39–63.
890 doi:[10.1144/GSL.SP.2004.221.01.04](https://doi.org/10.1144/GSL.SP.2004.221.01.04)

891 Gautheron, C., Tassan-Got, L., Barbarand, J. & Pagel, M. (2009) Effect of alpha-damage annealing
892 on apatite (U–Th)/He thermochronology. *Chemical Geology*, **266**, 157–170.
893 doi:[10.1016/j.chemgeo.2009.06.001](https://doi.org/10.1016/j.chemgeo.2009.06.001)

894 Goldstein, R.M., Zebker, H.A. & Werner, C.L. (1988) Satellite radar interferometry: Two-
895 dimensional phase unwrapping. *Radio Sci.*, **23**, 713–720. doi:[10.1029/RS023i004p00713](https://doi.org/10.1029/RS023i004p00713)

Grandin, R. (2015) Interferometric processing of SLC Sentinel-1 TOPS data, Presented at the FRINGE'15: Advances in the Science and Applications of SAR Interferometry and Sentinel-1 InSAR Workshop, Frascati, Italy, 23-27 March 2015.

Grandin, R., Vallée, M. & Lacassin, R. (2017) Rupture Process of the Mw5.8 Pawnee, Oklahoma, Earthquake from Sentinel-1 InSAR and Seismological Data. *Seismological Research Letters*, **88**, 994–1004. doi:[10.1785/0220160226](https://doi.org/10.1785/0220160226)

Gratier, J.-P., Thouvenot, F., Jenatton, L., Tourette, A., Doan, M.-L. & Renard, F. (2013) Geological control of the partitioning between seismic and aseismic sliding behaviours in active faults: Evidence from the Western Alps, France. *Tectonophysics*, **600**, 226–242. doi:[10.1016/j.tecto.2013.02.013](https://doi.org/10.1016/j.tecto.2013.02.013)

Grellet, B., Combes, P. & Granier, T. (1993) Sismotectonique de la France métropolitaine dans son cadre géologique et géophysique: avec atlas de 23 cartes au 1/4 000 000ème et une carte au 1/1 000 000ème, Société géologique de France.

Heidbach, O., Rajabi, M., Cui, X., Fuchs, K., Müller, B., Reinecker, J., Reiter, K., *et al.* (2018) The World Stress Map database release 2016: Crustal stress pattern across scales. *Tectonophysics*, **744**, 484–498. doi:[10.1016/j.tecto.2018.07.007](https://doi.org/10.1016/j.tecto.2018.07.007)

Illies, J.H. (1972) The Rhine graben rift system-plate tectonics and transform faulting. *Geophysical Surveys*, **1**, 27–60. doi:[10.1007/BF01449550](https://doi.org/10.1007/BF01449550)

Jolivet, R., Duputel, Z., Riel, B., Simons, M., Rivera, L., Minson, S.E., Zhang, H., *et al.* (2014) The 2013 Mw 7.7 Balochistan Earthquake: Seismic Potential of an Accretionary Wedge. *Bulletin of the Seismological Society of America*, **104**, 1020–1030. doi:[10.1785/0120130313](https://doi.org/10.1785/0120130313)

Jolivet, R., Grandin, R., Lasserre, C., Doin, M.-P. & Peltzer, G. (2011) Systematic InSAR tropospheric phase delay corrections from global meteorological reanalysis data: correcting InSAR with ERA-Interim. *Geophys. Res. Lett.*, **38**, n/a-n/a. doi:[10.1029/2011GL048757](https://doi.org/10.1029/2011GL048757)

Jolivet, R., Simons, M., Agram, P.S., Duputel, Z. & Shen, Z.-K. (2015) Aseismic slip and seismogenic coupling along the central San Andreas Fault. *Geophys. Res. Lett.*, **42**, 297–306. doi:[10.1002/2014GL062222](https://doi.org/10.1002/2014GL062222)

Jomard, H., Cushing, E.M., Palumbo, L., Baize, S., David, C. & Chartier, T. (2017) Transposing an active fault database into a seismic hazard fault model for nuclear facilities – Part 1: Building a database of potentially active faults (B DFA) for metropolitan France. *Nat. Hazards Earth Syst. Sci.*, **17**, 1573–1584. doi:[10.5194/nhess-17-1573-2017](https://doi.org/10.5194/nhess-17-1573-2017)

Kalifi, A., Leloup, P.-H., Sorrel, P., Galy, A., Demory, F., Spina, V., Huet, B., *et al.* (2021) Chronology of thrust propagation from an updated tectono-sedimentary framework of the Miocene molasse (western Alps). *Solid Earth Discuss.*, **2021**, 1–68, Copernicus Publications. doi:[10.5194/se-2021-46](https://doi.org/10.5194/se-2021-46)

Kerrien, Y., Elmi, S., Busnardo, R., Camus, G., Kieffer, G., Moinereau, J. & Weisbrod, A. (1989) Carte géologique de la France au 1/50000, feuille Aubenas (865), Bureau de Recherches Géologiques et Minières.

King, G. & Nabelek, J. (1985) Role of Fault Bends in the Initiation and Termination of Earthquake Rupture. *Science*, **228**, 984–987. doi:[10.1126/science.228.4702.984](https://doi.org/10.1126/science.228.4702.984)

Klinger, Y., Michel, R. & King, G. (2006) Evidence for an earthquake barrier model from Mw~7.8 Kokoxili (Tibet) earthquake slip-distribution. *Earth and Planetary Science Letters*, **242**, 354–364. doi:[10.1016/j.epsl.2005.12.003](https://doi.org/10.1016/j.epsl.2005.12.003)

939 Lacassin, R., Meyer, B., Benedetti, L., Armijo, R. & Tapponnier, P. (1998) Geomorphic evidence
 940 for Quaternary sinistral slip on the Cévennes Fault (Languedoc, France). *Comptes Rendus de*
 941 *l'Académie des Sciences Series IIA Earth and Planetary Science*, **11**, 807–815.

942 Lacassin, R., Meyer, B., Benedetti, L., Armijo, R. & Tapponnier, P. (1998) Réponse aux
 943 commentaires de Ambert et al., Mattauer et Sébrier et al. à la note: 'Signature morphologique de
 944 l'activité de la faille des Cévennes (Languedoc, France)'. *Comptes Rendus de l'Académie des*
 945 *Sciences-Series IIA-Earth and Planetary Science*, **327**, 861–866, Elsevier Masson.

946 Lajaunie, C., Courrioux, G. & Manuel, L. (1997) Foliation fields and 3D cartography in geology:
 947 Principles of a method based on potential interpolation. *Math Geol*, **29**, 571–584.
 948 doi:[10.1007/BF02775087](https://doi.org/10.1007/BF02775087)

949 Leonard, M. (2010) Earthquake Fault Scaling: Self-Consistent Relating of Rupture Length, Width,
 950 Average Displacement, and Moment Release. *Bulletin of the Seismological Society of America*,
 951 **100**, 1971–1988. doi:[10.1785/0120090189](https://doi.org/10.1785/0120090189)

952 Liu, F., Elliott, J.R., Craig, T.J., Hooper, A. & Wright, T.J. (2021) Improving the Resolving Power
 953 of InSAR for Earthquakes Using Time Series: A Case Study in Iran. *Geophys Res Lett*, **48**.
 954 doi:[10.1029/2021GL093043](https://doi.org/10.1029/2021GL093043)

955 Lohman, R.B. & Simons, M. (2005) Some thoughts on the use of InSAR data to constrain models
 956 of surface deformation: Noise structure and data downsampling. *Geochem. Geophys. Geosyst.*, **6**,
 957 doi:[10.1029/2004GC000841](https://doi.org/10.1029/2004GC000841)

958 López-Quiroz, P., Doin, M.-P., Tupin, F., Briole, P. & Nicolas, J.-M. (2009) Time series analysis of
 959 Mexico City subsidence constrained by radar interferometry. *Journal of Applied Geophysics*, **69**, 1–
 960 15. doi:[10.1016/j.jappgeo.2009.02.006](https://doi.org/10.1016/j.jappgeo.2009.02.006)

961 Lorenchet, D., Monjuvent, G., Bornad, M. & Combier, J. (1979) Carte géologique de la France au
 962 1/50000, feuille Montélimar (866), Bureau de Recherches Géologiques et Minières.

963 Loveless, J.P. & Meade, B.J. (2011) Spatial correlation of interseismic coupling and coseismic
 964 rupture extent of the 2011 Mw = 9.0 Tohoku-oki earthquake: COUPLING AND TOHOKU-OKI
 965 SLIP. *Geophys. Res. Lett.*, **38**, n/a-n/a. doi:[10.1029/2011GL048561](https://doi.org/10.1029/2011GL048561)

966 Manchuel, K., Traversa, P., Baumont, D., Cara, M., Nayman, E. & Durouchoux, C. (2018) The
 967 French seismic CATalogue (FCAT-17). *Bull Earthquake Eng*, **16**, 2227–2251. doi:[10.1007/s10518-017-0236-1](https://doi.org/10.1007/s10518-017-0236-1)

969 Marchandon, M., Hollingsworth, J. & Radiguet, M. (2021) Origin of the shallow slip deficit on a
 970 strike slip fault: Influence of elastic structure, topography, data coverage, and noise. *Earth and*
 971 *Planetary Science Letters*, **554**, 116696. doi:[10.1016/j.epsl.2020.116696](https://doi.org/10.1016/j.epsl.2020.116696)

972 Martin, P. & Bergerat, F. (1996) Palaeo-stresses inferred from macro- and microfractures in the
 973 Balazuc-1 borehole (GPF programme). Contribution to the tectonic evolution of the Cévennes
 974 border of the SE Basin of France. *Marine and Petroleum Geology*, **13**, 671–684. doi:[10.1016/0264-8172\(95\)00063-1](https://doi.org/10.1016/0264-8172(95)00063-1)

976 Masson, C., Mazzotti, S., Vernant, P. & Doerflinger, E. (2019) Extracting small deformation
 977 beyond individual station precision from dense Global Navigation Satellite System (GNSS)
 978 networks in France and western Europe. *Solid Earth*, **10**, 1905–1920. doi:[10.5194/se-10-1905-2019](https://doi.org/10.5194/se-10-1905-2019)

979 Mattauer, M., Lacassin, R., Meyer, B., Benedetti, L., Armijo, R. & Tapponnier, P. (1998)
 980 Commentaires à la note de R. Lacassin, B. Meyer, L. Benedetti, R. Armijo et P. Tapponnier.

981 ‘Signature morphologique de l’activité de la faille des Cévennes (Languedoc, France)’. *Comptes*
982 *Rendus de l’Académie des Sciences Series IIA Earth and Planetary Science*, **12**, 859.

983 Maubant, L., Pathier, E., Daout, S., Radiguet, M., Doin, M. -P., Kazachkina, E., Kostoglodov, V., *et*
984 *al.* (2020) Independent Component Analysis and Parametric Approach for Source Separation in
985 InSAR Time Series at Regional Scale: Application to the 2017–2018 Slow Slip Event in Guerrero
986 (Mexico). *J. Geophys. Res. Solid Earth*, **125**. doi:[10.1029/2019JB018187](https://doi.org/10.1029/2019JB018187)

987 Meade, B.J. (2007) Algorithms for the calculation of exact displacements, strains, and stresses for
988 triangular dislocation elements in a uniform elastic half space. *Computers & Geosciences*, **33**,
989 1064–1075. doi:[10.1016/j.cageo.2006.12.003](https://doi.org/10.1016/j.cageo.2006.12.003)

990 Mordret, A., Brenguier, F., Causse, M., Boué, P., Voisin, C., Dumont, I., Vernon, F.L., *et al.* (2020)
991 Seismic Stereometry Reveals Preparatory Behavior and Source Kinematics of Intermediate-Size
992 Earthquakes. *Geophys. Res. Lett.*, **47**. doi:[10.1029/2020GL088563](https://doi.org/10.1029/2020GL088563)

993 Pinel-Puysegur, B., Michel, R. & Avouac, J.-P. (2012) Multi-Link InSAR Time Series:
994 Enhancement of a Wrapped Interferometric Database. *IEEE J. Sel. Top. Appl. Earth Observations*
995 *Remote Sensing*, **5**, 784–794. doi:[10.1109/JSTARS.2012.2196758](https://doi.org/10.1109/JSTARS.2012.2196758)

996 Radiguet, M., Cotton, F., Vergnolle, M., Campillo, M., Valette, B., Kostoglodov, V. & Cotte, N.
997 (2011) Spatial and temporal evolution of a long term slow slip event: the 2006 Guerrero Slow Slip
998 Event: Evolution of the 2006 Guerrero SSE. *Geophysical Journal International*, **184**, 816–828.
999 doi:[10.1111/j.1365-246X.2010.04866.x](https://doi.org/10.1111/j.1365-246X.2010.04866.x)

1000 Ritz, J.-F., Baize, S., Ferry, M., Hannouz, E., Riesner, M., Bollinger, L., Larroque, C., *et al.* (2021)
1001 Analyzing the paleoseismic history of the La Rouvière fault, unexpected source of the 11-11-2019,
1002 Mw4.9 Le Teil surface rupturing earthquake (Cévennes fault system, France), Presented at the EGU
1003 General Assembly 2021, EGU. doi:[10.5194/egusphere-egu21-13044](https://doi.org/10.5194/egusphere-egu21-13044)

1004 Ritz, J.-F., Baize, S., Ferry, M., Larroque, C., Audin, L., Delouis, B. & Mathot, E. (2020) Surface
1005 rupture and shallow fault reactivation during the 2019 Mw 4.9 Le Teil earthquake, France. *Commun*
1006 *Earth Environ*, **1**, 10. doi:[10.1038/s43247-020-0012-z](https://doi.org/10.1038/s43247-020-0012-z)

1007 Rosen, P.A., Hensley, S., Peltzer, G. & Simons, M. (2004) Updated repeat orbit interferometry
1008 package released. *Eos Trans. AGU*, **85**, 47–47. doi:[10.1029/2004EO050004](https://doi.org/10.1029/2004EO050004)

1009 Roure, F., Brun, J.-P., Colletta, B. & Van Den Driessche, J. (1992) Geometry and kinematics of
1010 extensional structures in the alpine foreland basin of southeastern France. *Journal of Structural*
1011 *Geology*, **14**, 503–519. doi:[10.1016/0191-8141\(92\)90153-N](https://doi.org/10.1016/0191-8141(92)90153-N)

1012 Roure, F., Brun, J.P., Colletta, B. & Vially, R. (1994) Multiphase Extensional Structures, Fault
1013 Reactivation, and Petroleum Plays in the Alpine Foreland Basin of Southeastern France. in
1014 *Hydrocarbon and Petroleum Geology of France* ed. Mascle, A., pp. 245–268, Berlin, Heidelberg:
1015 Springer Berlin Heidelberg. doi:[10.1007/978-3-642-78849-9_18](https://doi.org/10.1007/978-3-642-78849-9_18)

1016 Saint Martin, M. (2009) Carte géologique harmonisée de l’Ardèche, Bureau de Recherches
1017 Géologiques et Minières.

1018 Sanchis, E. & Séranne, M. (2000) Structural style and tectonic evolution of a polyphase extensional
1019 basin of the Gulf of Lion passive margin: the Tertiary Alès basin, southern France. *Tectonophysics*,
1020 **322**, 219–242. doi:[10.1016/S0040-1951\(00\)00097-4](https://doi.org/10.1016/S0040-1951(00)00097-4)

1023 Sébrier, M, Bellier, O., Peulvast, J. & Vergély, P. (1998) Commentaires à la note de R. Lacassin, B.
1024 Meyer, L. Benedetti, R. Armijo et P. Tapponnier. ‘Signature morphologique de l’activité de la faille
1025 des Cévennes (Languedoc, France)’. *Comptes Rendus de l’Académie des Sciences Series IIA Earth*
1026 *and Planetary Science*, **12**, 855–856.

1027 Sébrier, Michel, Ghafiri, A. & Bles, J.-L. (1997) Paleoseismicity in France: Fault trench studies in a
1028 region of moderate seismicity. *Journal of Geodynamics*, **24**, 207–217. doi:[10.1016/S0264-](https://doi.org/10.1016/S0264-3707(97)00005-7)
1029 [3707\(97\)00005-7](https://doi.org/10.1016/S0264-3707(97)00005-7)

1030 Séranne, M., Benedicto, A., Labaum, P., Truffert, C. & Pascal, G. (1995) Structural style and
1031 evolution of the Gulf of Lion Oligo-Miocene rifting: role of the Pyrenean orogeny. *Marine and*
1032 *Petroleum Geology*, **12**, 809–820. doi:[10.1016/0264-8172\(95\)98849-Z](https://doi.org/10.1016/0264-8172(95)98849-Z)

1033 Soechting, W. (1996) Etude et modélisation de la fracturation de la partie septentrionale de la
1034 bordure viva-ro-cévenole autour de Privas (entre La Voulte-sur-Rhône et Aubenas), Ardèche,
1035 Université Lyon 1.

1036 Sudhaus, H. & Jónsson, S. (2009) Improved source modelling through combined use of InSAR and
1037 GPS under consideration of correlated data errors: application to the June 2000 Kleifarvatn
1038 earthquake, Iceland. *Geophysical Journal International*, **176**, 389–404. doi:[10.1111/j.1365-](https://doi.org/10.1111/j.1365-246X.2008.03989.x)
1039 [246X.2008.03989.x](https://doi.org/10.1111/j.1365-246X.2008.03989.x)

1040 Tarantola, A. (2005) Inverse problem theory and methods for model parameter estimation, SIAM.

1041 Thouvenot, F., Jenatton, L. & Gratier, J.-P. (2009) 200-m-deep earthquake swarm in Tricastin
1042 (lower Rhône Valley, France) accounts for noisy seismicity over past centuries. *Terra Nova*, **21**,
1043 203–210. doi:[10.1111/j.1365-3121.2009.00875.x](https://doi.org/10.1111/j.1365-3121.2009.00875.x)

1044 Vallage, A., Bollinger, L., Champenois, J., Duverger, C., Trilla, A.G., Hernandez, B., Pichon, A.L.,
1045 *et al.* (2021) Multitechnology characterization of an unusual surface rupturing intraplate
1046 earthquake: the *M* L 5.4 2019 Le Teil event in France. *Geophysical Journal International*, **226**,
1047 803–813. doi:[10.1093/gji/ggab136](https://doi.org/10.1093/gji/ggab136)

1048 Walters, R.J., Gregory, L.C., Wedmore, L.N.J., Craig, T.J., McCaffrey, K., Wilkinson, M., Chen, J.,
1049 *et al.* (2018) Dual control of fault intersections on stop-start rupture in the 2016 Central Italy
1050 seismic sequence. *Earth and Planetary Science Letters*, **500**, 1–14. doi:[10.1016/j.epsl.2018.07.043](https://doi.org/10.1016/j.epsl.2018.07.043)

1051 Wells, D.L. & Coppersmith, K.J. (1994) New empirical relationships among magnitude, rupture
1052 length, rupture width, rupture area, and surface displacement. *Bulletin of the Seismological Society*
1053 *of America*, **84**, 974–1002.

1054 Wesnousky, S.G. (2006) Predicting the endpoints of earthquake ruptures. *Nature*, **444**, 358–360.
1055 doi:[10.1038/nature05275](https://doi.org/10.1038/nature05275)

1056 Xu, X., Tong, X., Sandwell, D.T., Milliner, C.W.D., Dolan, J.F., Hollingsworth, J., Leprince, S., *et*
1057 *al.* (2016) Refining the shallow slip deficit. *Geophys. J. Int.*, **204**, 1843–1862.
1058 doi:[10.1093/gji/ggv563](https://doi.org/10.1093/gji/ggv563)

1059

1060 **Supplementary Material**

1061

1062

1063 The 3D geological model can be downloaded at
1064 https://zenodo.org/record/5974794#.Yf_USC_pPUI.
1065 (To open with Adobe Acrobat Reader)

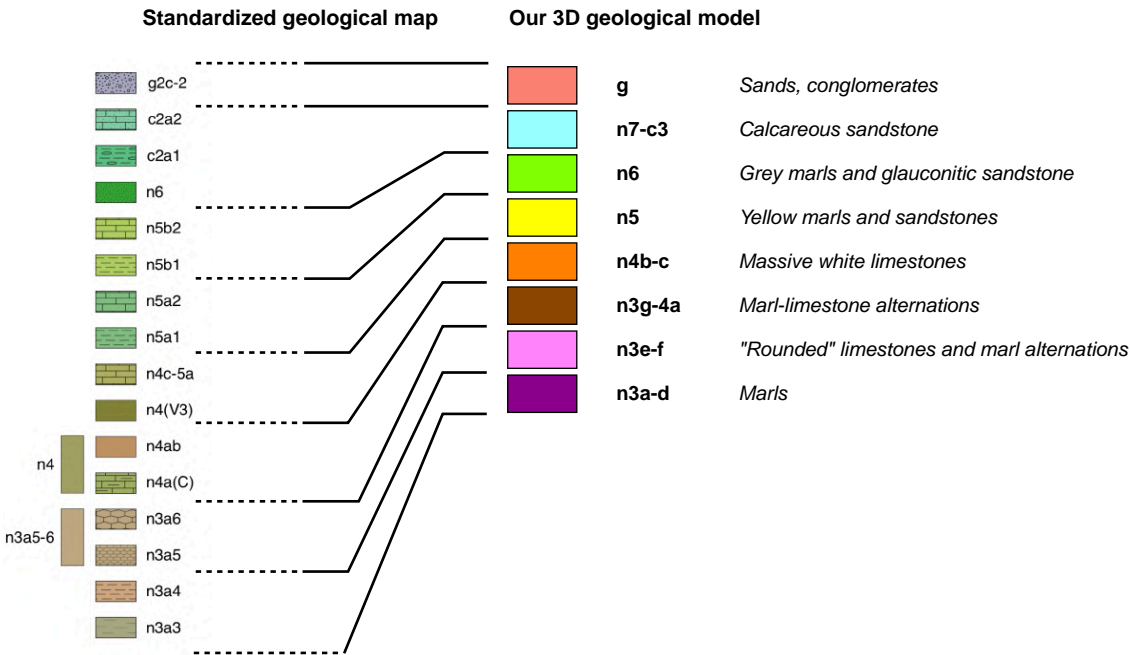
1066

1067

1068

1069

1070



1071

1072 **Figure S1.** Correspondence of stratigraphic logs between published geological maps, and our 3D model, for
1073 units outcropping in the 3D model zone.

1074

1075

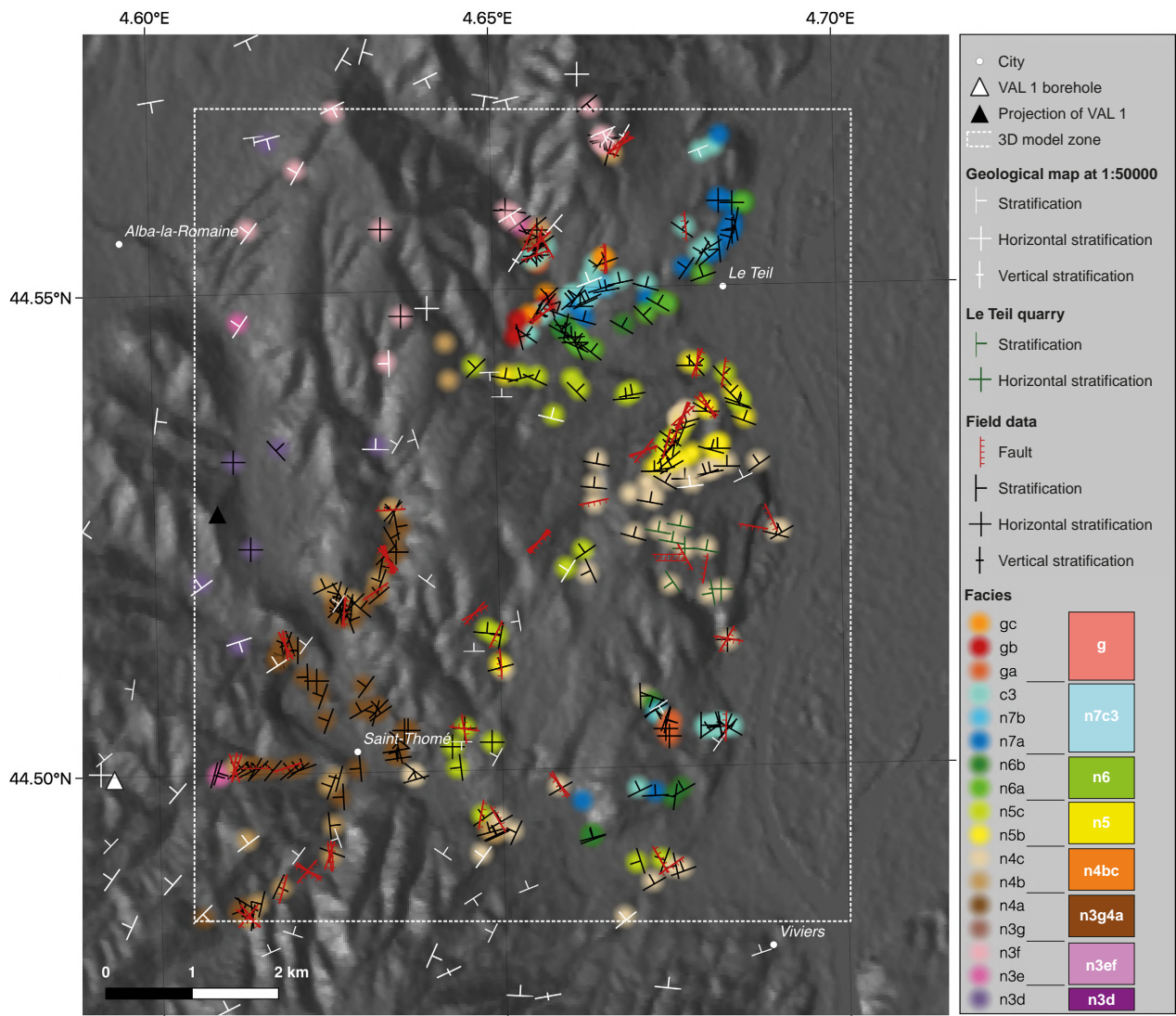
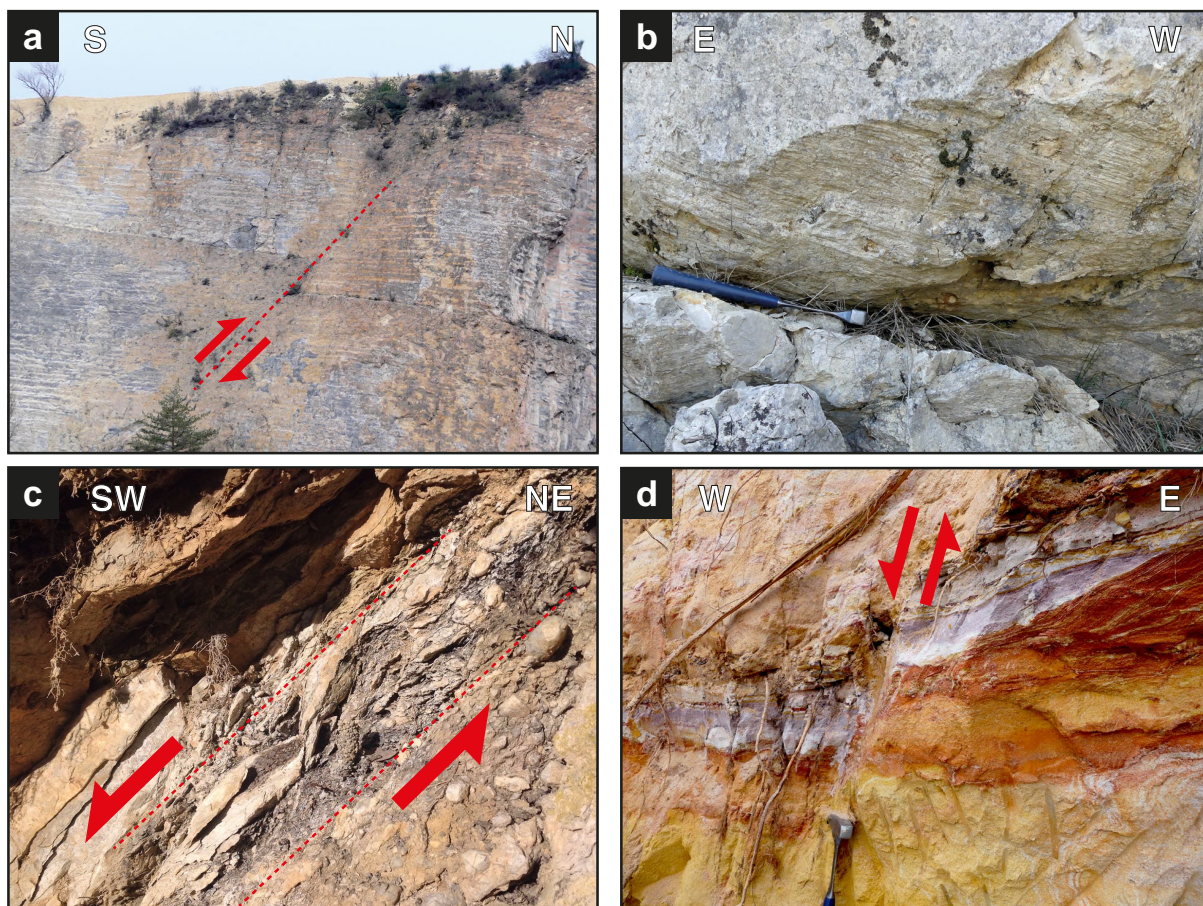


Figure S2. Complete data set used as input for 3D geological modeling.



1082

1083 **Figure S3.** Additional field observations. (a) [Site LT123] Thrust fault in barremian limestones, striking
 1084 ~N100 and offsetting a stratigraphic level by a few meters. (b) [Site LT62] Fault plane showing strike-slip
 1085 slickensides in limestones. (c) [Site LT59] Shear zone oriented ~N150 with C-S criteria suggesting a partially
 1086 normal faulting. (d) [Site LT29] Normal fault in typical Oligocene colored sands, with 17 cm offset. Sites'
 1087 location is shown in Fig. S7.

1088

1089

1090

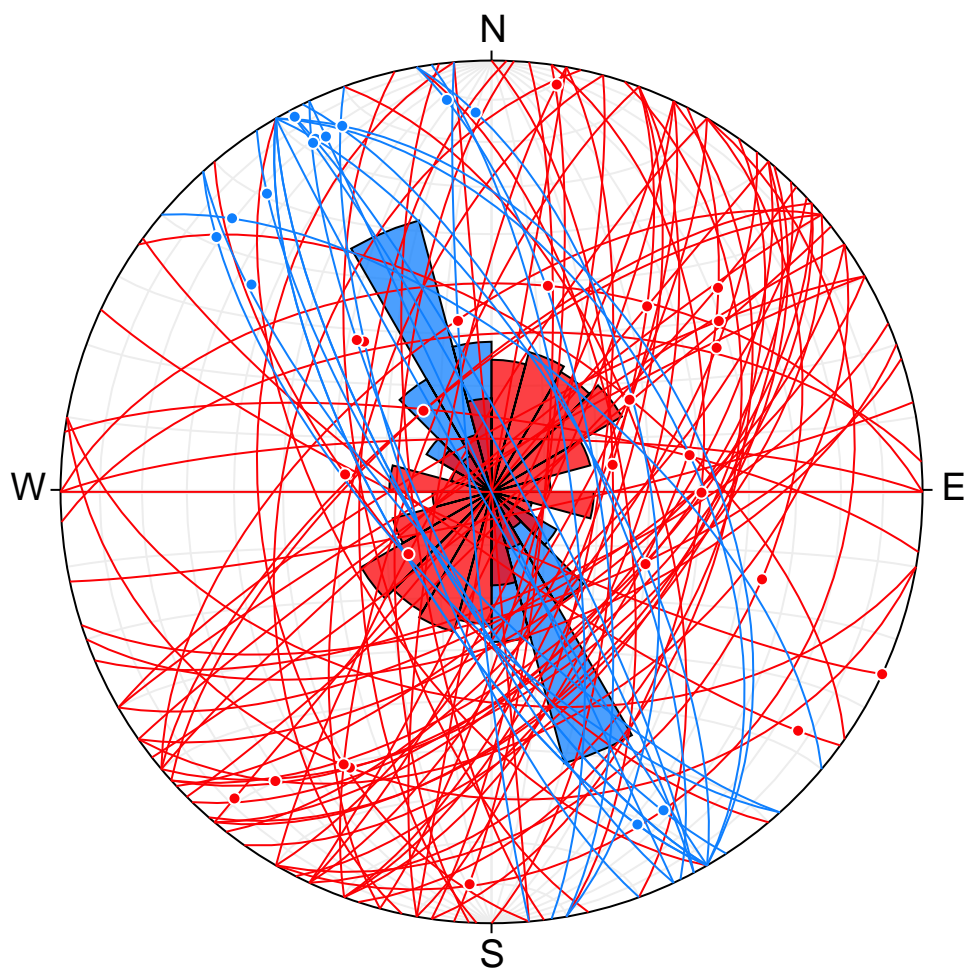


Figure S4. Stereonet of all fault field measurements. The ~N150 strike-slip faults are in blue. All other faults measured are in red. Fig. 5(c) shows only the measurements corresponding to La Rouvière fault.

VAL 1 BOREHOLE				INTERPRETATION FOR 3D MODEL			
Absolute depth (bottom)	Relative depth (bottom)	Thickness	Formation	Thickness	Formation	General facies	Remarks
-147	0		Surface		n3ef		
547	694	694	HAUTERIVIAN	694	n3ad	Marls with clayey limestone layers Glauconitic at bottom	Thickness not consistent with the geological map, which describes a max. thickness of 850 for the whole n3 unit. Despite that, we keep borehole thickness.
765	912	218	VALANGINIAN	890	n2	Marls with clayey limestone layers	Thickness largely under-estimated in this borehole because of a fault. Corrected using geological map description
803	950	38	BERRIASIAN	358	j6n1	Limestones, marl layers	
886	1033	83	TITHONIAN				
927	1074	41	KIMMERIDGIAN				
1123	1270	196	LUSITANIAN				
1205	1352	82	OXFORDIAN	389	j25	Marls, black clays	
1436	1583	231	CALLOVIAN				
1512	1659	76	BATHONIAN				
1925	2072	413	BAJOCIAN	413	j1	Clayey limestones and calcareous marls alternations	
3228	3375	1303	Upper LIAS SUP. (Toarcian-Aalenian)	1303	Lias	Marls, marl-limestone alternations	Uncertainties on the thicknesses.
3422	3569	194	Middle LIAS (Carixian-Domerian)	194	156	Marnes, marnes claires	NOT IN THE MODEL
3953	4100	531	Lower LIAS (Hettangian-Sinemurian)	531	114	Clayey limestones	
			TRIASSIC				

Figure S5. VAL 1 borehole interpretation. The borehole is located at 4.5935°E, 44.4997°N.

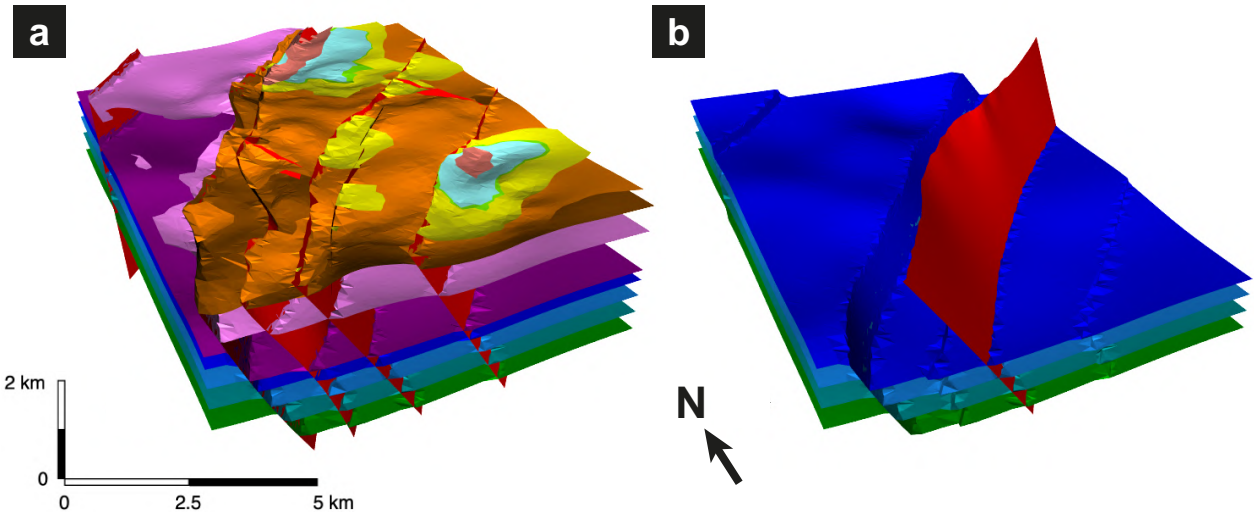


Figure S6. 3D view of the geological model. Color code for units as in Fig. 2. (a) Complete view. (b) Truncated view to highlight La Rouvière Fault geometry.

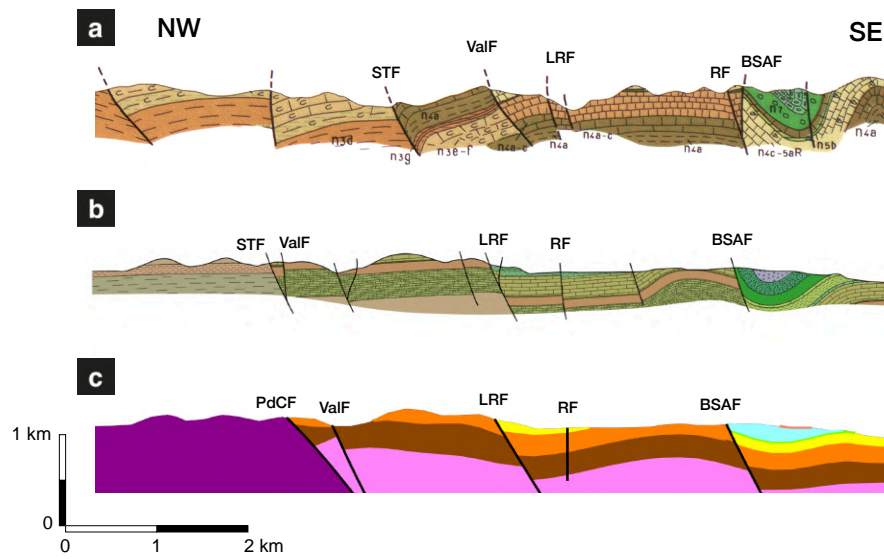
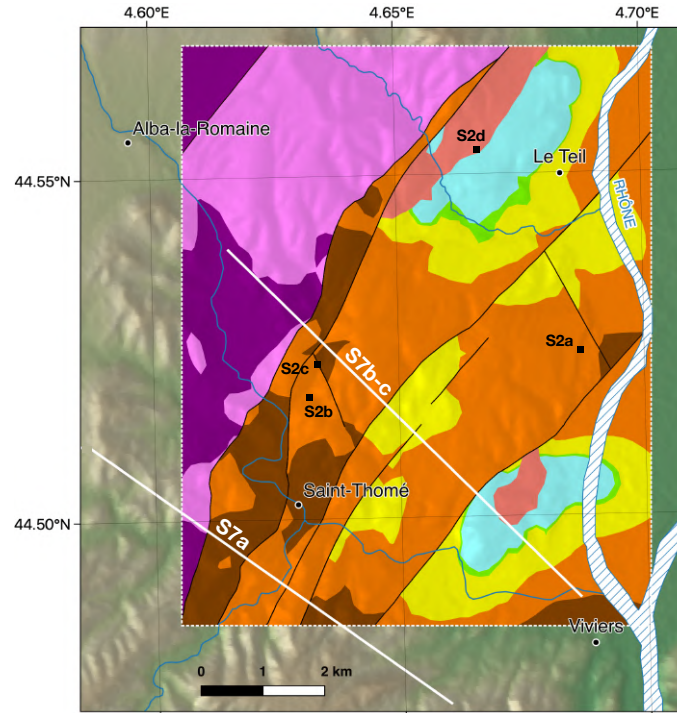


Figure S7. Comparison of published and this study geological cross-sections. (a) Cross-section published in the Aubenas 1:50000 geological map (Kerrien et al. 1979), located SW of the 3D model zone. (b) Cross-section made from the standardized 1:50000 geological map (Saint Martin, 2009), across the 2019 Le Teil rupture on LRF. (c) Cross section made from our 3D geological model, along the same trace than b. We refer to Aubenas geological map for stratigraphic description of a, stratigraphy of b and c is shown in Fig. S1. *PdCF*: Pontet-de-Couloubre fault; *STF*: Saint-Thomé fault; *ValF*: Valgayette fault *LRF*: La Rouvière fault; *RF*: Rocherenard fault; *BSAF*: Bayne-St-Alban fault.

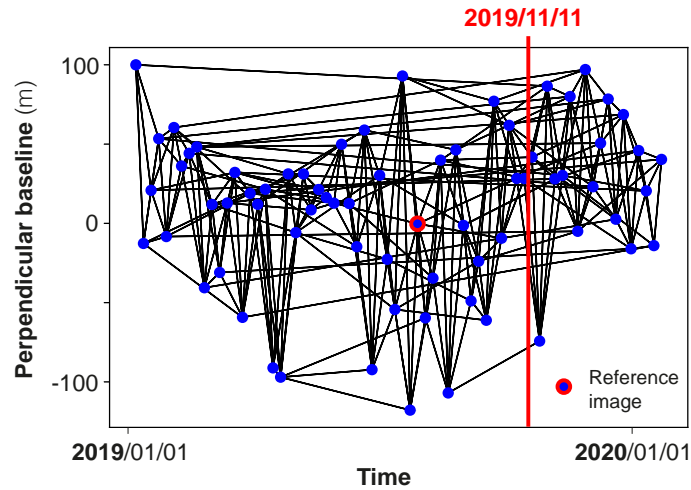


Figure S8. Relative perpendicular baseline as a function of time for SAR images (blue dots with reference image in red) and interferograms (black lines) network used in time series analysis.

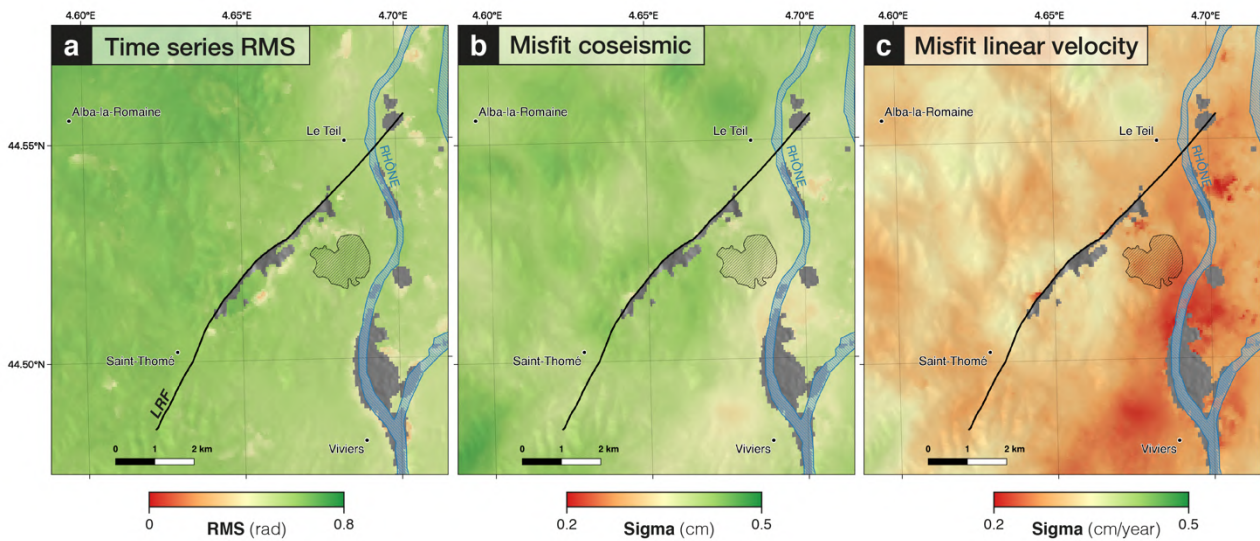
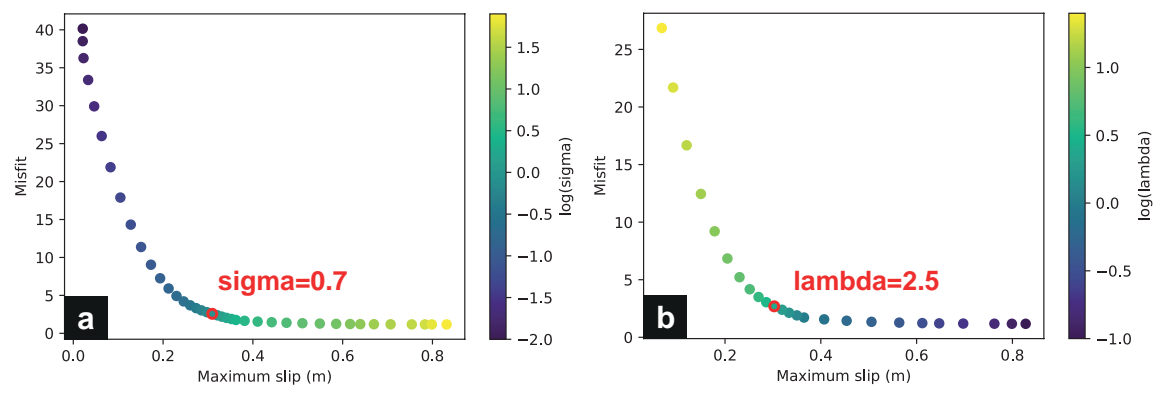


Figure S9. Uncertainties associated with the InSAR times series. (a) Root Mean Square misclosure of the time series inversion averaged per pixel. (b) and (c) Misfits from the temporal decomposition of the time series, relative to the estimations of the coseismic step and the linear velocity, respectively.

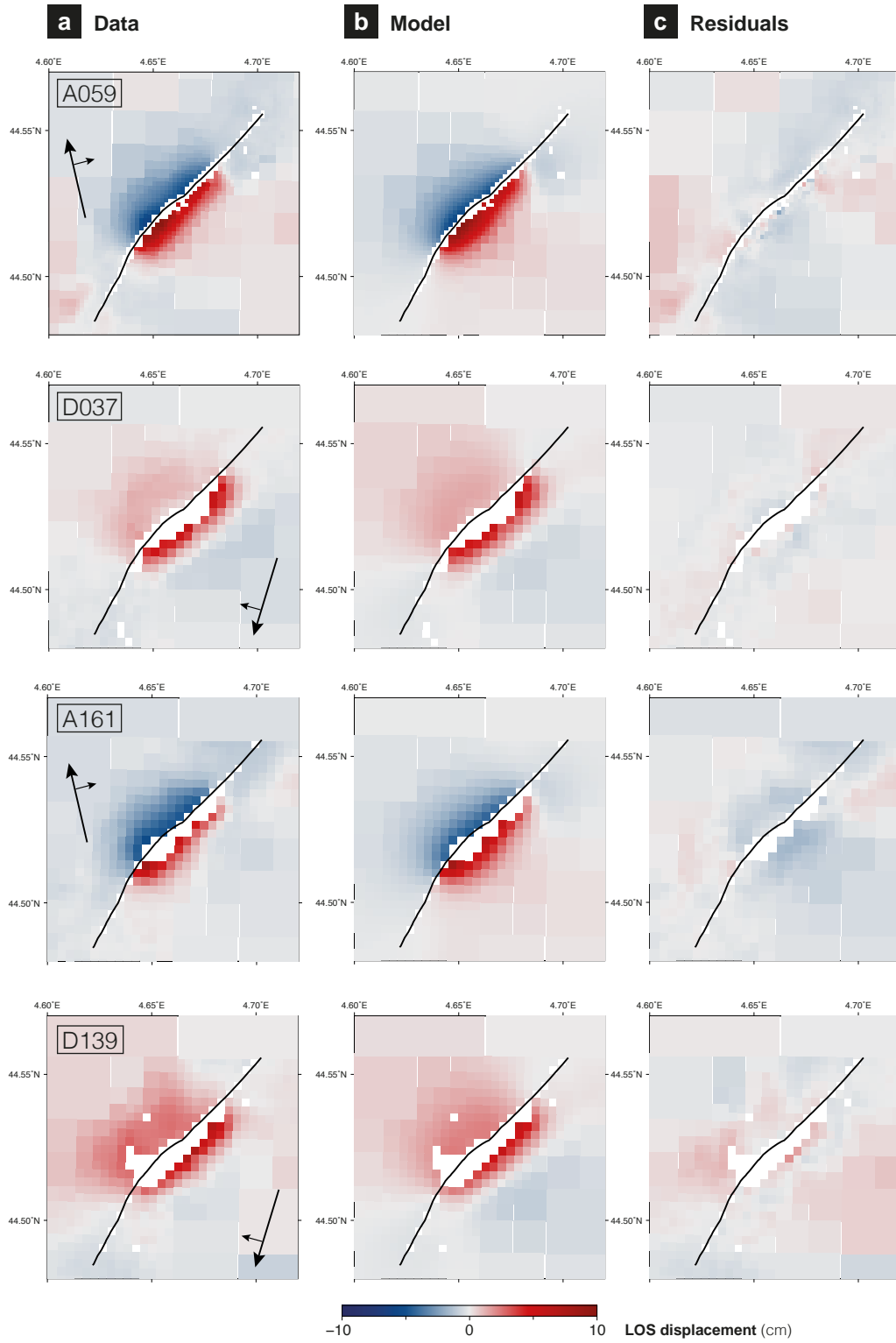
1125



1126

1127 **Figure S10.** Exploration of regularization parameters used in slip inversion (see text for details).

1128



1129

1130 **Figure S11.** Left (a) : Downsampled coseismic InSAR displacement field (derived from time series analysis
 1131 on top or single interferograms at middle and bottom); center (b) : modelled surface displacement; and right (c)
 1132 : residuals for best fitting model.

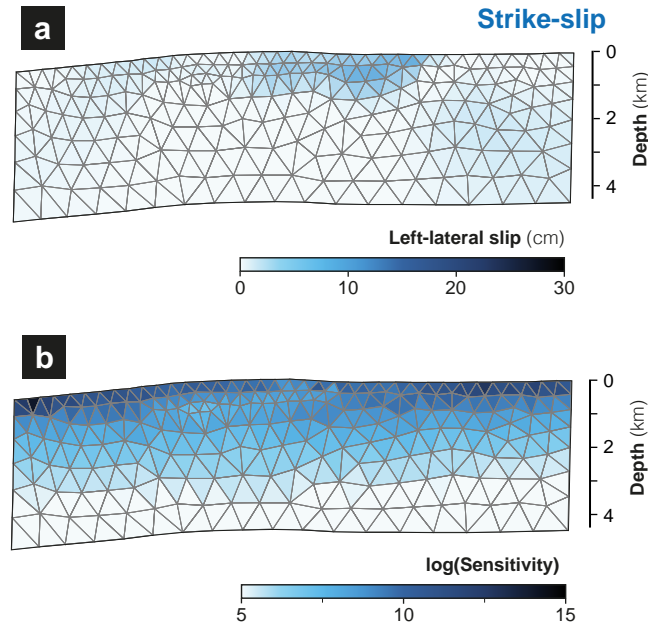


Figure S12. Slip distribution and inversion sensitivity for strike-slip component.

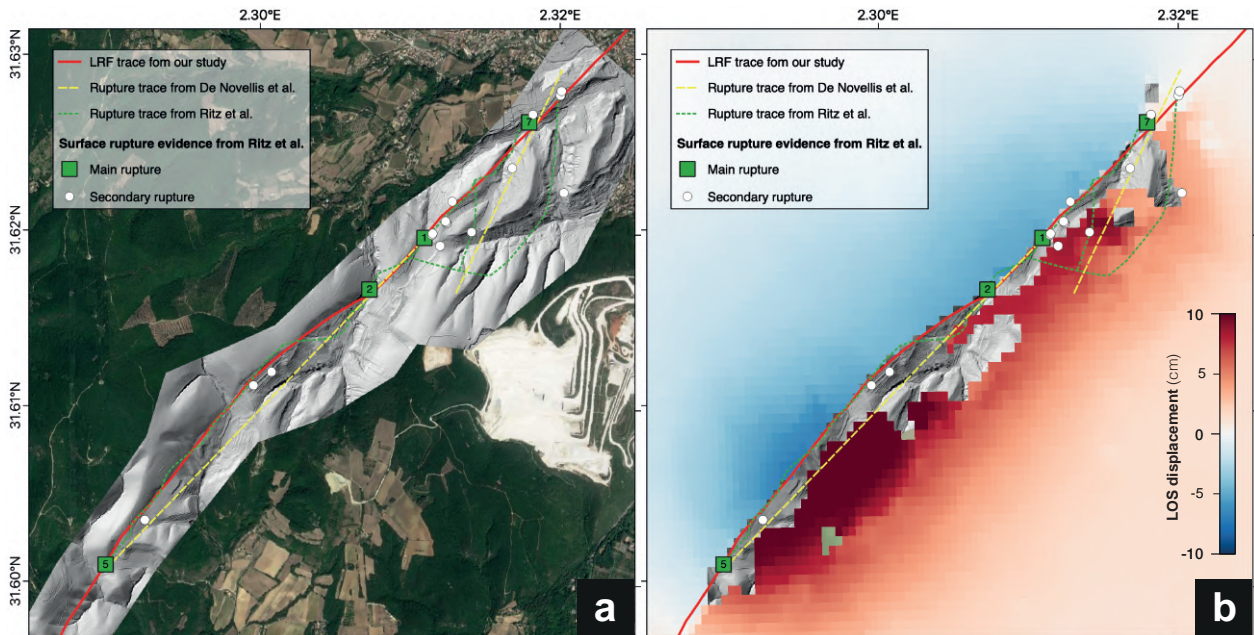


Figure S13. Comparison of different rupture traces already published, from field or InSAR measurements : green squares, white dots and dashed blue lines from Ritz et al. (2020); yellow dashed line from DeNovellis et al. (2020); with the surface rupture trace used in this study (red line). Rupture traces superimposed (a) on satellite image (source) and LiDAR topographic map (source) and (b) coseismic displacement field from this study.

1142 **References**

1143 De Novellis, V., Convertito, V., Valkaniotis, S., Casu, F., Lanari, R., Monterroso Tobar, M.F. & Pino, N.A. (2020)
1144 Coincident locations of rupture nucleation during the 2019 Le Teil earthquake, France and maximum stress change
1145 from local cement quarrying. *Commun Earth Environ*, **1**, 20. doi:[10.1038/s43247-020-00021-6](https://doi.org/10.1038/s43247-020-00021-6)

1146 Kerrien, Y., Elmi, S., Busnardo, R., Camus, G., Kieffer, G., Moinereau, J. & Weisbrod, A. (1989) Carte géologique de
1147 la France au 1/50000, feuille Aubenas (865), Bureau de Recherches Géologiques et Minières.

1148 Ritz, J.-F., Baize, S., Ferry, M., Larroque, C., Audin, L., Delouis, B. & Mathot, E. (2020) Surface rupture and shallow
1149 fault reactivation during the 2019 Mw 4.9 Le Teil earthquake, France. *Commun Earth Environ*, **1**, 10.
1150 doi:[10.1038/s43247-020-0012-z](https://doi.org/10.1038/s43247-020-0012-z)